

# BESIII Analysis Memo

DocDB-817

BAM-817

August 16, 2019

## Amplitude Analysis and Branching Fraction Measurement of

$$D_s^+ \rightarrow K^+ K^- \pi^+$$

Meng Wang<sup>a</sup>, Yu Lu<sup>a</sup>, and Liaoyuan Dong<sup>a</sup>, and Huaimin Liu<sup>a</sup><sup>a</sup>*Institute of High Energy Physics, CAS*

## Internal Referee Committee

Ref1 xx (Chair)<sup>d</sup>, Ref2 xx<sup>e</sup>, and Ref3 xx<sup>f</sup><sup>d</sup>*Department of Computer Science and Engineering*<sup>e</sup>*Department of Electrical Engineering*<sup>f</sup>*Latex Univeristy*DocDB : <http://docbes3.ihep.ac.cn/cgi-bin/DocDB/ShowDocument?docid=817>Hypernews : <http://hnb3.ihep.ac.cn/HyperNews/get/paper817.html>

## Abstract

We report the amplitude analysis and branching fraction measurement of  $D_s^+ \rightarrow K^+ K^- \pi^+$  decay using a data sample of  $3.19 \text{ fb}^{-1}$  recorded with BESIII detector at a center-of-mass energy of 4.178 GeV. We perform a model-independent partial wave analysis (MIPWA) in the low  $K^+ K^-$  region to extract the  $K^+ K^-$   $S$ -wave lineshape. We also perform an amplitude analysis on a nearly background free sample of 4399 events to investigate the substructure, and determine the relative fractions and the phases among the different intermediate processes. The amplitude analysis results provide an accurate detection efficiency and allow measurement of the branching fraction of  $D_s^+ \rightarrow K^+ K^- \pi^+$  to be  $\mathcal{B}(D_s^+ \rightarrow K^+ K^- \pi^+) = (5.47 \pm 0.07_{\text{stat.}} \pm 0.13_{\text{sys.}})\%$ .

# Contents

<b>1</b>	<b>1 Introduction</b>	<b>3</b>
1.1	The Scalar Meson $f_0(980)$ and $a_0(980)$ . . . . .	3
1.2	The Dynamics of the Strong Interaction . . . . .	4
1.3	Amplitude Analysis . . . . .	5
<b>2</b>	<b>Data Set and Monte Carlo Samples</b>	<b>6</b>
<b>3</b>	<b>Event Selection</b>	<b>7</b>
3.1	Tracking, PID, $\pi^0$ , $\eta$ , $\eta'$ and $K_S^0$ Reconstruction . . . . .	7
3.2	$D_s$ Selection . . . . .	8
3.3	Signal Selection . . . . .	9
<b>4</b>	<b>Partial Wave Analysis in the Low <math>K^+K^-</math> Mass Region</b>	<b>10</b>
4.1	Event Selection . . . . .	10
4.2	Background Analysis . . . . .	10
4.3	Partial Wave Analysis . . . . .	15
4.4	S-wave Parameterization at the $K^+K^-$ Threshold . . . . .	16
<b>5</b>	<b>Amplitude Analysis</b>	<b>18</b>
5.1	Event Selection . . . . .	18
5.2	Background Analysis . . . . .	18
5.3	Fit Method . . . . .	19
5.3.1	Propagator . . . . .	21
5.3.2	Blatt-Weisskopf Barriers . . . . .	21
5.3.3	Spin Factors . . . . .	22
5.4	Fit Fraction . . . . .	22
5.5	Fit Result . . . . .	22
5.6	Systematic Uncertainties . . . . .	26
<b>6</b>	<b>Branching Fraction Measurements</b>	<b>30</b>
6.1	Event Selection . . . . .	30
6.2	Analytic Strategy . . . . .	30
6.3	Results of Branching Fraction . . . . .	33
6.4	Systematic Uncertainties . . . . .	33

<sup>1</sup> **7 Summary**

# 1 Introduction

The Cabibbo-favored (CF)  $D_s^+ \rightarrow K^+ K^- \pi^+$  decay has a large branching fraction and low background contamination. This decay is, therefore, usually suited as a reference channel for other decays of the  $D_s$  meson and used as normalization for decay chains involving charm quarks. An accurate knowledge of its substructure is important to reduce systematic uncertainties in analyses using this channel. The study of intermediate processes in this decay can also illuminates light meson spectroscopy and shed light on different production mechanisms.

## 1.1 The Scalar Meson $f_0(980)$ and $a_0(980)$

The Constituent Quark Model has been very successful in the past few decades by explaining how hadrons are made up. Based on this model, the nonets of pseudo-scalar, vector, and tensor mesons are now well identified. However, the identification of the scalar mesons is still uncertain due to the broad widths and the lack of a distinctive angular distribution. Among the candidates for the spin-parity  $J^{PC} = 0^{++}$  nonet, the parameters of some states such as  $f_0(980)$  and  $a_0(980)$  are not well measured,

Recently, the decay  $D_s^+ \rightarrow a_0(980)^0 \pi^+$  has been observed through  $D_s^+ \rightarrow \pi^+ \pi^0 \eta$  [1]. The overlap of  $f_0(980)$  and  $a_0(980)$  make it very difficult to distinguish them. From the Dalitz plot analysis of  $D_s^+ \rightarrow \pi^+ \pi^- \pi^+$ , we can get the branching fraction  $\mathcal{B}(D_s^+ \rightarrow f_0(980) \pi^+, f_0(980) \rightarrow \pi^+ \pi^-)$ . With the branching ratio of  $\Gamma_{f_0(980)}(K^+ K^-)/\Gamma_{f_0(980)}(\pi^+ \pi^-)$ , we can obtain:

$$\mathcal{B}(D_s^+ \rightarrow f_0(980) \pi^+, f_0(980) \rightarrow K^+ K^-) = \mathcal{B}(D_s^+ \rightarrow f_0(980) \pi^+, f_0(980) \rightarrow \pi^+ \pi^-) \frac{\Gamma_{f_0(980)}(K^+ K^-)}{\Gamma_{f_0(980)}(\pi^+ \pi^-)}. \quad (1)$$

In a similar way, we can obtain:

$$\mathcal{B}(D_s^+ \rightarrow a_0(980) \pi^+, a_0(980) \rightarrow K^+ K^-) = \mathcal{B}(D_s^+ \rightarrow a_0(980) \pi^+, a_0(980) \rightarrow \pi^0 \eta) \frac{\Gamma_{a_0(980)}(K^+ K^-)}{\Gamma_{a_0(980)}(\pi^0 \eta)}. \quad (2)$$

So the ratio of fit fractions between  $\mathcal{R}$  of  $D_s^+ \rightarrow f_0(980) \pi^+$  and  $D_s^+ \rightarrow a_0(980) \pi^+$  is:

$$\mathcal{R} = \frac{\mathcal{B}(D_s^+ \rightarrow f_0(980) \pi^+, f_0(980) \rightarrow \pi^+ \pi^-) \frac{\Gamma_{f_0(980)}(K^+ K^-)}{\Gamma_{f_0(980)}(\pi^+ \pi^-)}}{\mathcal{B}(D_s^+ \rightarrow a_0(980) \pi^+, a_0(980) \rightarrow \pi^0 \eta) \frac{\Gamma_{a_0(980)}(K^+ K^-)}{\Gamma_{a_0(980)}(\pi^0 \eta)}}. \quad (3)$$

The confirmation of the value  $\mathcal{R}$  in Eq. 3 can help to fix the ratio in amplitude analyses and then distinguish  $f_0(980)$  and  $a_0(980)$  at the low end of  $K^+ K^-$  mass spectrum. Using isospin relations, the relation between  $\Gamma_{f_0(980)}(\pi\pi)/\Gamma_{f_0(980)}(\pi\pi + K\bar{K})$  and  $\Gamma_{f_0(980)}(K^+ K^-)/\Gamma_{f_0(980)}(\pi^+ \pi^-)$  is:

$$\frac{\Gamma_{f_0(980)}(K^+ K^-)}{\Gamma_{f_0(980)}(\pi^+ \pi^-)} = \frac{3}{4} \cdot \left[ \frac{1}{\frac{\Gamma_{f_0(980)}(\pi\pi)}{\Gamma_{f_0(980)}(\pi\pi) + \Gamma_{f_0(980)}(K\bar{K})}} - 1 \right]. \quad (4)$$

1 However, the value of  $\Gamma_{f_0(980)}(K^+K^-)/\Gamma_{f_0(980)}(\pi^+\pi^-)$  is not well measured, shown in Table 1.  $f_0(980)$  is  
 2 very close to  $K\bar{K}$  threshold and has strong coupling to  $\pi\pi$  and  $K\bar{K}$  final states. So we perform a model-  
 3 independent partial wave analysis (MIPWA) to extract the  $S$  wave lineshape in the low end of  $K^+K^-$   
 4 mass spectrum. In this analysis, we use  $S(980)$  to denote the  $a_0(980)$  and  $f_0(980)$  resonances.

Table 1: The  $f_0(980)$  branching ratio  $\Gamma_{f_0(980)}(\pi\pi)/[\Gamma_{f_0(980)}(\pi\pi) + \Gamma_{f_0(980)}(K\bar{K})]$

value	Collaboration	comment
$0.52 \pm 0.12$	BABAR	$B^\pm \rightarrow K^\pm \pi^\pm \pi^\mp$ [2]
$0.75^{+0.11}_{-0.13}$	BESII	$\chi_{c0} \rightarrow 2\pi^+ 2\pi^-, \pi^+ \pi^- K^+ K^-$ [3]
$0.84 \pm 0.02$	SPEC	Combined fit [4]

## 5 1.2 The Dynamics of the Strong Interaction

6 Hadronic decays of charmed mesons are important for understanding the dynamics of the strong  
 7 interaction in the low energy regime. Fig. 1 illustrates main Feynman diagrams related to the  $D_s^+ \rightarrow$   
 $K^+K^-\pi^+$  decay. Experimental measurements can help to refine theoretical models [5] [6] [7].

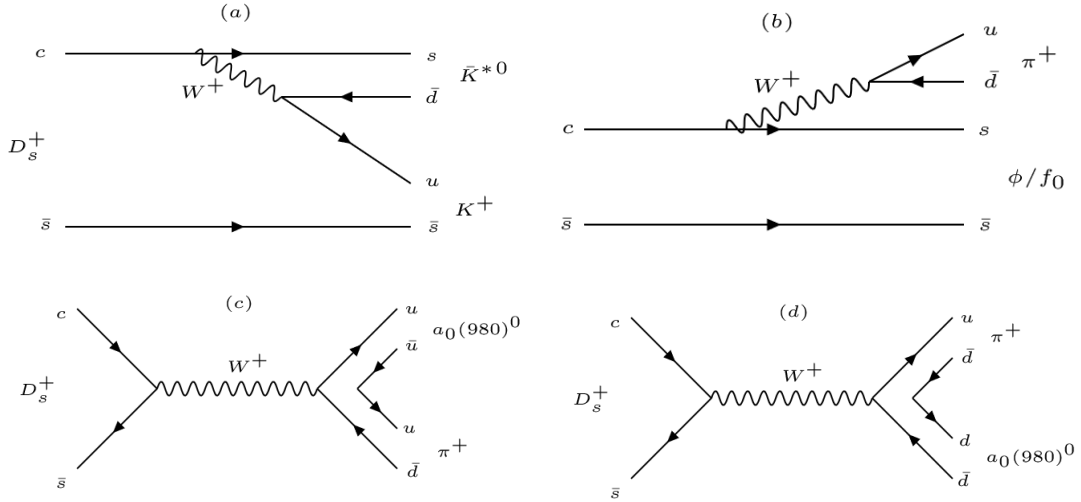


Figure 1: Main decay diagrams associated with  $D_s^+ \rightarrow K^+K^-\pi^+$  decay. The main contribution comes from the tree diagram with an internal  $W^+$  emission (Fig. 1(a)), that describes the  $D_s^+ \rightarrow \bar{K}^*(892)^0 K^+$  decay, the diagram with an external  $W^+$  emission (Fig. 1(b)), that describes the diagram  $D_s^+ \rightarrow \phi\pi^+/f_0\pi^+$ , and the diagram with  $W$ -annihilation (Fig. 1(c) and Fig. 1(d)), that describes the decay  $D_s \rightarrow a_0(980)^0\pi^+$ .

### 1.3 Amplitude Analysis

Knowledge of the substructure in  $D_s^+ \rightarrow K^+ K^- \pi^+$  decay allows us to properly determine the detection efficiency when measuring its branching fraction. Dalitz plot analyses of this decay have been performed by the E687 [8], CLEO [9] and Babar [10] collaborations. E687 used about 700 events and did not take  $f_0(1370)\pi^+$  into account. For CLEO-c, about 14400 events with purity about 84.9% were selected with the single tag method. The analysis of BABAR used about 100000 events with purity about 95%. Table 2 shows the comparison of the fitted decay fractions with the Dalitz plot analyses of previous analyses.

Table 2: Comparison between Babar, CLEO-c and E687 Dalitz plot analysis.

Decay mode	Fit fraction(BABAR)	Fit fraction(CLEO-c)	Fit fraction(E687)
$D_s^+ \rightarrow \bar{K}^*(892)^0 K^+$	$47.9 \pm 0.5 \pm 0.5$	$47.4 \pm 1.5 \pm 0.4$	$47.8 \pm 4.6 \pm 4.0$
$D_s^+ \rightarrow \phi(1020)\pi^+$	$41.4 \pm 0.8 \pm 0.5$	$42.2 \pm 1.6 \pm 0.3$	$39.6 \pm 3.3 \pm 4.7$
$D_s^+ \rightarrow S(980)\pi^+$	$16.4 \pm 0.7 \pm 2.0$	$28.2 \pm 1.9 \pm 1.8$	$11.0 \pm 3.5 \pm 2.6$
$D_s^+ \rightarrow \bar{K}_0^*(1430)^0 K^+$	$2.4 \pm 0.3 \pm 1.0$	$3.9 \pm 0.5 \pm 0.5$	$9.3 \pm 3.2 \pm 3.2$
$D_s^+ \rightarrow f_0(1710)\pi^+$	$1.1 \pm 0.1 \pm 0.1$	$3.4 \pm 0.5 \pm 0.3$	$3.4 \pm 2.3 \pm 3.5$
$D_s^+ \rightarrow f_0(1370)\pi^+$	$1.1 \pm 0.1 \pm 0.2$	$4.3 \pm 0.6 \pm 0.5$	...
$\sum FF(\%)$	$110.2 \pm 0.6 \pm 2.0$	$129.5 \pm 4.4 \pm 2.0$	111.1
$\chi^2/NDF$	$\frac{2843}{2305-14} = 1.2$	$\frac{178}{117} = 1.5$	$\frac{50.2}{33} = 1.5$
Events	$96307 \pm 369$	$12226 \pm 22$	$701 \pm 36$

From Table 2, we can see an obvious difference of decay fraction of  $f_0(980)\pi^+$  between BABAR and CLEO-c. In this analysis with the double tag method, we can get a nearly background free data sample, which is good to perform the amplitude analysis.

## 2 Data Set and Monte Carlo Samples

We use  $3.195 \text{ fb}^{-1}$  data set collected at  $E_{cm} = 4.178 \text{ GeV}$  by BESIII detector in 2016. Both data sample and Monte Carlo samples are reconstructed under BOSS7.0.3. All samples were generated with run-dependent  $E_{cm}$  [12], except for the Bhabha,  $\mu$ -pair and Two-photon fusion events. For these three types of events, we used a constant  $E_{cm}$  at 4178.37 MeV, which is twice of a luminosity-weighted average of the measured beam energy in the center-of-mass frame. Total 40 rounds of generic MC with each round equaling to data size are used for background study, tag efficiencies estimation (rounds 01-30) and input-output check for branching fraction measurement (rounds 31-40). They are available at /besfs3/offline/data/703-1/4180/mc/. For each round of generic MC, the detail components and corresponding size of each Monte Carlo sample are given in Table 3.

Table 3: Component and corresponding sizes, assume luminosity = 3195/pb.

Component	cross section (pb)	Size (M)	directory
$D^0 D^0$	179	0.5719	D0D0
$D^+ D^-$	197	0.6294	DpDm
$D^{*0} D^0$	1211	3.8691	DST0D0
$D^{*+} D^-$	1296	4.1407	DSTpDm
$D^{*0} D^{*0}$	2173	6.9427	DST0DST0
$D^{*+} D^{*-}$	2145	6.8533	DSTpDSTm
$D_s^+ D_s^-$	7	0.0225	DsDs
$D_s^{*+} D_s^-$	961	3.0700	DsSTDs
$DD^* \pi^+$	383	1.2237	DDSTPIp
$DD^* \pi^0$	192	0.6134	DDSTPI0
$DD \pi^+$	50	0.1598	DDPIp
$DD \pi^0$	25	0.0799	DDPI0
Component	cross section (nb)	Size (M)	directory
$q\bar{q}$	13.8	44.0910	qq
$\gamma J/\psi$	0.40	1.2780	RR1S
$\gamma \psi(2S)$	0.42	1.3419	RR2S
$\gamma \psi(3770)$	0.06	0.1917	RR3770
$\tau\tau$	3.45	11.0228	tt
$\mu\mu$	5.24	16.7418	mm
$ee$	423.99	13.5465(0.01×)	ee
Two-photon fusion	1.7	5.4315	TwoGam
HCT	0.10178	0.3252	HCT

For the Signal MC, we generate the signal events with one  $D_s$  decaying to signal mode using the generator “DIY”, in which the parameters are obtained from the fit to data. phase space (PHSP) MC and Signal MC are used in MC integration required for the amplitude fit. The Signal MC is also used in the input/output check.

### 3 Event Selection

At  $E_{cm} = 4.178$  GeV, pairs of  $D_s D_s^*$  are produced, and the  $D_s^*$  decays to either  $D_s \gamma$  or  $D_s \pi^0$ . So the  $D_s^*$  mesons are produced in pairs without additional charged hadrons ( $K^\pm(\pi^\pm)$ ). We do not search for the gamma or  $\pi^0$  from the  $D_s$  decay. These unique  $D_s^+ D_s^-$  final states provide us an opportunity to employ the double tag method to measure the absolute branching fractions of  $D_s$  meson decays. The double tag method also provide clean samples to perform an amplitude analysis.

#### 3.1 Tracking, PID, $\pi^0$ , $\eta$ , $\eta'$ and $K_S^0$ Reconstruction

$D_s$  candidates are built from  $K^\pm$ ,  $\pi^\pm$ ,  $\pi^0$ ,  $\eta$ ,  $\eta'$  and  $K_S^0$ . The selections of the particles to build  $D_s$  candidates are performed with DTagAlg-00-01-05 package with the default setting, which are summarized below.

- Tracking:

- The properties of charged tracks are determined based on the MDC information. Charged track candidates must satisfy:

- $|\cos\theta| < 0.93$ ,

- $|dr| < 1$  cm and  $|dz| < 10$  cm,

where  $|dr|$  and  $|dz|$  are defined as the one reconstructed minus the interaction point.

- Particle ID:

- Charged tracks are identified as pions or kaons with Particle Identification (PID), which is implemented by combing the information of the energy loss ( $dE/dx$ ) in MDC and the time-of-flight measured from the TOF system. Kaon and Pion are identified with the requirements that

- $Prob(K) > 0$  and  $Prob(K) > Prob(\pi)$  for  $K$ ,

- $Prob(\pi) > 0$  and  $Prob(\pi) > Prob(K)$  for  $\pi$ , where  $Prob(X)$  is the probability of hypothesis X, X can be  $\pi$  or  $K$ .

- $\pi^0/\eta$  selection:  $\pi^0/\eta$  candidates are reconstructed through  $\pi^0 \rightarrow \gamma\gamma$  ( $\eta \rightarrow \gamma\gamma$ ) with package of PioEtaToGGRecAlg.

The photons are reconstructed as energy showers on the EMC. We require:

- Minimum energy for barrel showers ( $|\cos\theta| < 0.8$ ):  $E_{min} > 25 \text{ MeV}/c^2$ ,



- Minimum energy for endcap showers ( $0.86 < |\cos\theta| < 0.92$ ):  $E_{min} > 50 \text{ MeV}/c^2$ ,
- Shower within other  $|\cos\theta|$  regions are rejected,
- EMC time requirements for events with at least one charged track detected:  $0 \leq t \leq 14$  (50 ns).

Then we perform a constrained fit on the photon pairs to the nominal  $\pi^0/\eta$  mass and require:

- The unconstrained invariant mass for  $\pi^0$ :  $0.115 < M(\gamma\gamma) < 0.015 \text{ GeV}/c^2$ ,
  - The unconstrained invariant mass for  $\eta$ :  $0.490 < M(\eta) < 0.580 \text{ GeV}/c^2$ ,
  - Mass fit:  $\chi^2_{1c} < 30$ .
- $\eta'$  selection: The  $\eta'$  candidates are reconstructed with  $\pi^+\pi^-\eta$ , the invariant mass for  $\pi^+\pi^-\eta$  is required to fall into the range of  $[0.938, 0.978] \text{ GeV}/c^2$ .
  - $K_S^0$  selection:  $K_S^0$  candidates are reconstructed using VeeVertexAlg package with two opposite charged tracks with requiring:
    - $|\cos\theta| < 0.93$ ,
    - $|dz| < 20 \text{ cm}$ .

For each pair of tracks, a constrained vertex fit is performed and the track parameters' results are used to get the invariant mass  $M(K_S^0)$ . Then the decay length of  $K_S^0$  is obtained with second vertex fit by the SecondVertexFit package. For  $K_S^0$  selection, we require:

- $0.487 \text{ GeV}/c^2 < M(K_S^0) < 0.511 \text{ GeV}/c^2$ ,
- Significance of the  $K_S^0$  decay length has two standard deviations.

### 3.2 $D_s$ Selection

The  $D_s$  candidates are constructed from individual  $\pi$ , K,  $\eta$ ,  $\eta'$ ,  $K_S^0$  and  $\pi^0$  in an event. The  $D_s$  candidates fall into the mass window of  $1.87 < m_{D_s} < 2.06 \text{ GeV}/c^2$  and the corresponding  $M_{rec}$  satisfied  $2.051 < M_{rec} < 2.180 \text{ GeV}/c^2$  are retained for further study. The definition of  $M_{rec}$  is

$$M_{rec} = \sqrt{(E_{cm} - \sqrt{p_{D_s}^2 + m_{D_s}^2})^2 - |\vec{p}_{cm} - \vec{p}_{D_s}|^2}, \quad (5)$$

where  $E_{cm}$  is the energy of initial state calculated from the beam energy [12],  $\vec{p}_{D_s}$  is the momentum of  $D_s$  candidate,  $m_{D_s}$  is  $D_s$  mass quoted from PDG [13], and  $\vec{p}_{cm}$  and  $\vec{p}_{D_s}$  are four-momentum of the initial state and the decay products of the  $D_s$  candidate, respectively.

### 1   **3.3   Signal Selection**

2        We use different methods to select events in the model independent analysis (Sec. [4.1](#)), the amplitude  
3   analysis (Sec. [5.1](#)) and the branching fraction measurement (Sec. [6.1](#)).

## 4 Partial Wave Analysis in the Low $K^+K^-$ Mass Region

In the  $K^+K^-$  threshold, both  $a_0(980)$  and  $f_0(980)$  can be present, and both resonances have very similar parameters which suffer from large uncertainties. In this section we obtain the model-independent information on the  $K^+K^-S$  wave by performing a partial wave analysis (PWA) in the  $K^+K^-$  threshold region.

### 4.1 Event Selection

After the selection in Sec. 3, we select signals for the model independent partial wave analysis. To retain enough statistics, we decide to use the single-tag method, and only to fully reconstruct one  $D_s^+ \rightarrow K^+K^-\pi^+$  in each event. We vote the candidates with  $\pi^\pm$  ( $\pi^0$ ) whose momentum is less than 0.1 GeV to remove soft  $\pi^\pm$  ( $\pi^0$ ) from  $D^*$  decays. For each  $D_s$  candidate, all daughter tracks are added to apply a 1C kinematic fit constraining the mass of  $D_s$ . Then we select the best candidate with minimum  $\chi_{1c}^2$ .

### 4.2 Background Analysis

In order to suppress the background, the multiple-variable analysis (MVA) is used. We train MVA separately with different sets of variables for the two event categories depending on the  $D_s^+$  origin. Sideband region used below is defined as the region of  $1.90 < M(D_s) < 1.952 \text{ GeV}/c^2$  and  $1.985 < M(D_s) < 2.03 \text{ GeV}/c^2$ , where  $M(D_s)$  is the invariant mass of  $D_s$ , and the signal region is  $1.952 < M(D_s) < 1.985 \text{ GeV}/c^2$ . Two categories of events are selected in a  $M_{rec} - \Delta M$  2D plane as shown in Fig. 2.

- Cat. #0: Direct  $D_s^+$ . We use the following variables whose distributions for signal and background are shown in Fig. 3 for generic MC and Fig. 4 for data,

1.  $M_{rec}$ ,
2.  $P_{rest}$ , defined as the total momentum of the tracks and neutrals in the rest of event (not part of the  $D_s^+ \rightarrow K^+K^-\pi^+$  candidate),
3.  $E_\gamma$ , defined as the energy of gamma from  $D_s^*$ .

From Fig. 3 and Fig. 4, we can see that the corresponding distributions of these variables of data and generic MC are roughly consistent.

- Cat. #1: Indirect  $D_s^+$ . We use the following variables whose distributions for signal and background are shown in Fig. 5 for generic MC and Fig. 6 for data,

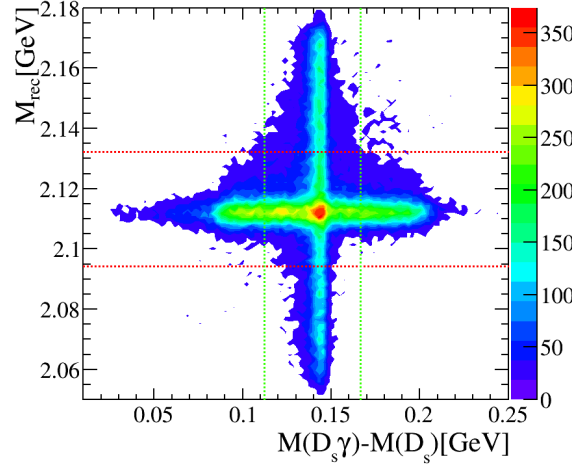


Figure 2: Two dimensional plane of  $M_{rec}$  versus  $\Delta M \equiv M(D_s^+ \gamma) - M(D_s^+)$  from the simulated  $D_s^+ \rightarrow K^+ K^- \pi^+$  decays. The red (green) dashed lines mark the mass window for the  $D_s^+$  Cat. #0 ( Cat. #1) around the  $M_{rec}$  ( $\Delta M$ ) peak.

1.  $\Delta M$ ,

2.  $M'_{rec}$ , defined as  $M'_{rec} = \sqrt{(E_{cm} - \sqrt{p_{D_s \gamma}^2 + m_{D_s^*}^2})^2 - p_{D_s \gamma}^2}$ , with  $p_{D_s \gamma}$  as the momentum of the  $D_s \gamma$  combination,  $m_{D_s^*}$  as the nominal  $D_s^*$  mass,

3.  $N_{tracks}$ , defined as the total number of tracks and neutrals in an event.

From Fig. 5 and Fig. 6, we can see that the corresponding distributions of these variables of data and generic MC are roughly consistent.

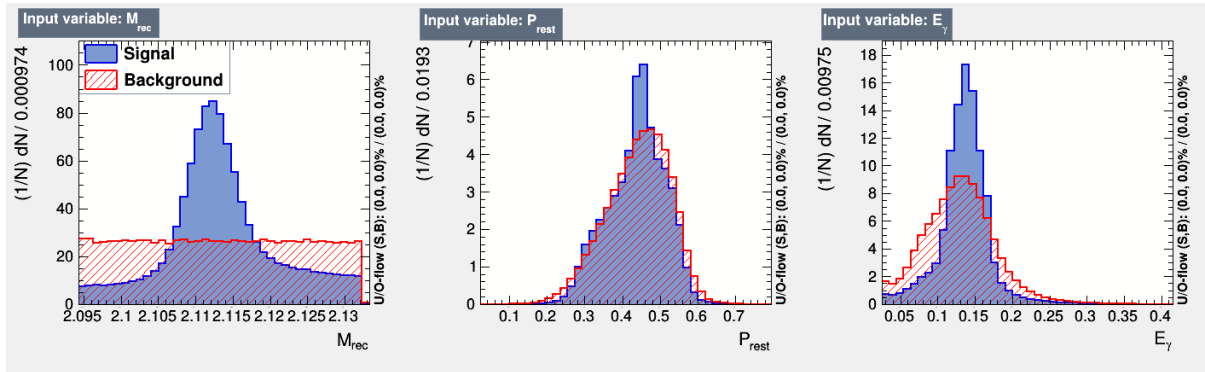


Figure 3: For event Cat. #0, distributions of MVA variables from simulated signal decays and background events.

As the results shown in Fig. 7, BDTG training and test samples are well matched. For event Cat. #0 ( Cat. #1 ), the sample with BDTG value larger than 0.33 (0.65) is retained for further study.

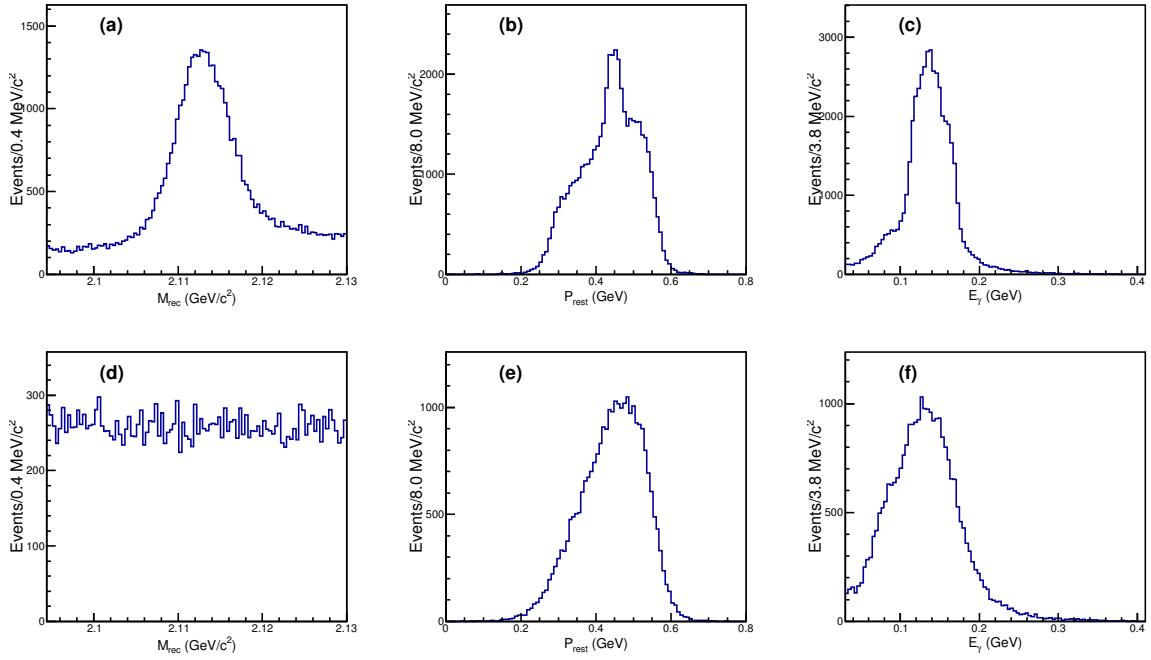


Figure 4: The distributions (Cat. #0) of these three observables ((a) and (d))  $M_{rec}$ , ((b) and (e))  $P_{rest}$  and ((c) and (f))  $E_\gamma$  for ( (a), (b) and (c)) signal and ( (d), (e) and (f)) sideband regions of data.

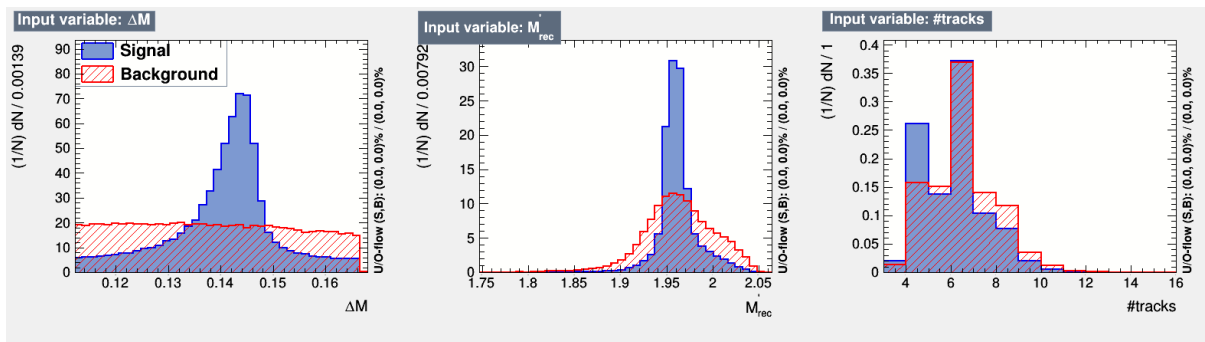


Figure 5: For event Cat. #1, distributions of MVA variables from simulated signal decays and background events.

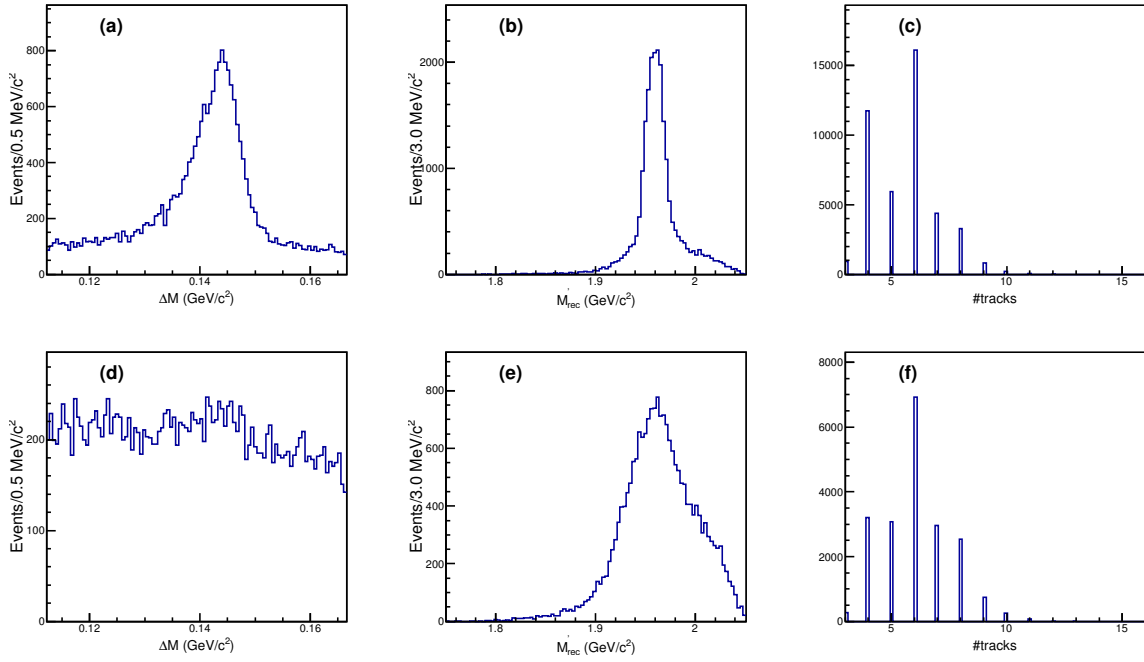


Figure 6: The distributions (Cat. #1) of these three observables ((a) and (d))  $M_{rec}$ , ((b) and (e))  $P_{rest}$  and ((c) and (f))  $E_\gamma$  for ( (a), (b) and (c)) signal and ( (d), (e) and (f)) sideband regions from data.

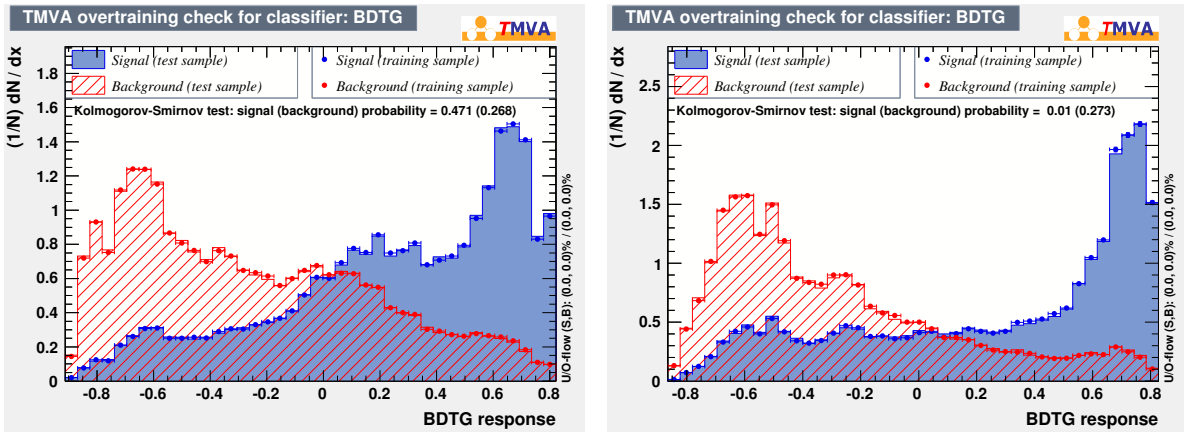


Figure 7: The comparisons between the training and test samples. The plot at left (right) is the comparison of Cat. #0 (Cat. #1).

After applying the BDTG requirement, the background shows no obviously peak around the region of  $[1.95, 1.982] \text{ GeV}/c^2$  (Signal region), which are shown in Fig. 8. The fit to the signal  $D_s$  invariant mass gives the background yield in Signal region is  $73.6 \pm 18.7$ , shown as in Fig. 9. In the fit, the signal shape is the MC shape convoluted with a Gaussian function and the background is described with 1<sup>st</sup>-order Chebychev polynomial.

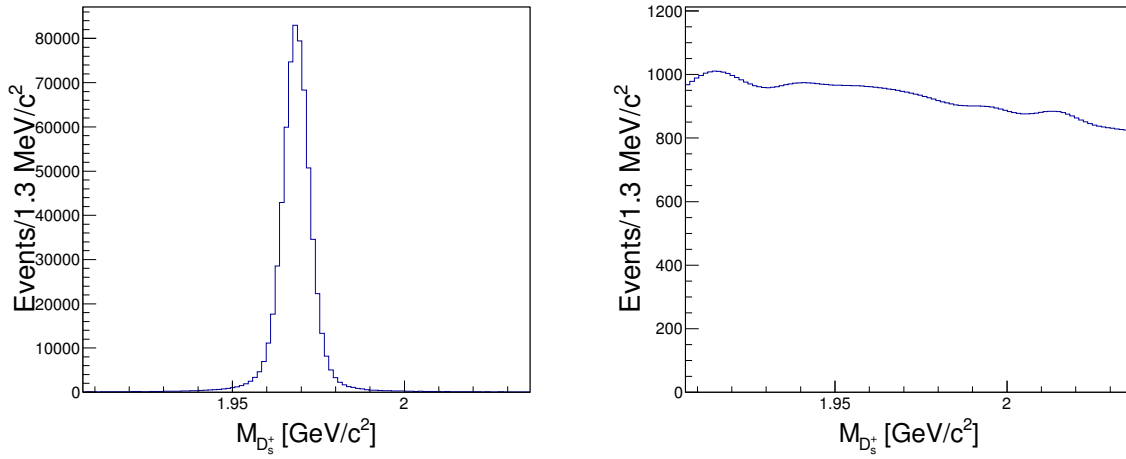


Figure 8: The signal and background distributions from generic MC after BDTG requirement.

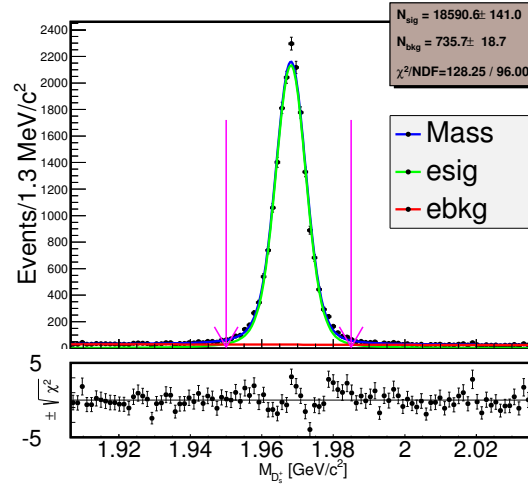


Figure 9: The fit to the signal  $D_s$  invariant mass ( $M_{D_s}$ ) spectrum after BDTG requirement, the area between the pink arrows is the signal area of the sample for MIPWA.

The projections of the “sideband” ( $1.90 < M(D_s) < 1.95 \text{ GeV}/c^2$  and  $1.985 < M(D_s) < 2.03 \text{ GeV}/c^2$ ) from data and generic MC with signal events removed are shown in Fig. 10. The corresponding plots agree well.

Thus the generic MC sample with signal events removed is used to subtract the background in data.

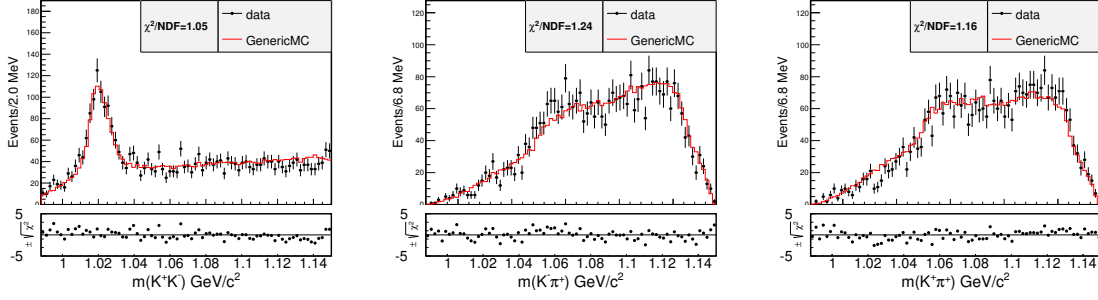


Figure 10: The projections of  $m(K^+K^-)$ ,  $m(K^-\pi^+)$ ,  $m(K^+\pi^+)$  from "Sideband" for data (dots with error bars) and generic MC with signal events removed (red histogram) after BDTG requirement.

### 4.3 Partial Wave Analysis

Assuming  $N$  is the number of events for a given mass interval  $I = [m_{K^+K^-}; m_{K^+K^-} + dm_{K^+K^-}]$ , we write the corresponding angular distributions in terms of the appropriate spherical harmonic functions is written

$$\frac{dN}{d\cos\theta} = 2\pi \sum_{k=0}^L \langle Y_k^0 \rangle Y_k^0(\cos\theta), \quad (6)$$

where  $L = 2\ell_{\max}$ , and  $\ell_{\max}$  is the maximum orbital angular momentum quantum number required to describe the  $K^+K^-$  system at  $m_{K^+K^-}$  (e.g.  $\ell_{\max}=1$  for S-, P-wave description);  $\theta$  is the angle between the direction of  $K^+$  and that of the  $K^+K^-$  system in the  $D_s^+$  rest frame. The normalizations are

$$\int_{-1}^1 Y_k^0(\cos\theta) Y_j^0(\cos\theta) d\cos\theta = \frac{\delta_{kj}}{2\pi}, \quad (7)$$

and it is assumed that the distribution  $\frac{dN}{d\cos\theta}$  has been efficiency corrected and background subtracted. Using this orthogonality condition, the coefficients in the expansion are obtained from

$$\langle Y_k^0 \rangle = \int_{-1}^1 \frac{dN}{d\cos\theta} Y_k^0(\cos\theta) d\cos\theta. \quad (8)$$

This integral is given, to a good approximation, by  $\sum_{n=1}^N Y_k^0(\cos\theta_n)$ , where  $\theta_n$  is the value of  $\theta$  for the  $n$ -th event.

Fig. 11 shows the  $K^+K^-$  mass spectrum up to  $1.15 \text{ GeV}/c^2$  weighted by  $Y_k^0(\cos\theta) = \sqrt{(2k+1)/(4\pi)} P_k(\cos\theta)$  for  $k=0, 1$ , and  $2$ , where  $P_k$  is the Legendre polynomial function of order  $k$ . These distributions are corrected for efficiency and phase space, and background is subtracted by background from generic MC after BDTG requirement.

The number of events  $N$  for the mass interval  $I$  can be expressed in terms of the partial-wave amplitudes describing the  $K^+K^-$  system. Assuming that only S- and P-wave amplitudes are necessary in this limited region, we can write:

$$\frac{dN}{d\cos\theta} = 2\pi |S Y_0^0(\cos\theta) + P Y_1^0(\cos\theta)|^2. \quad (9)$$



1 By comparing Eq. 6 and 9, we obtain

$$\begin{aligned}\sqrt{4\pi}\langle Y_0^0 \rangle &= |S|^2 + |P|^2, \\ \sqrt{4\pi}\langle Y_2^0 \rangle &= \frac{2}{\sqrt{5}} |P|^2,\end{aligned}\tag{10}$$

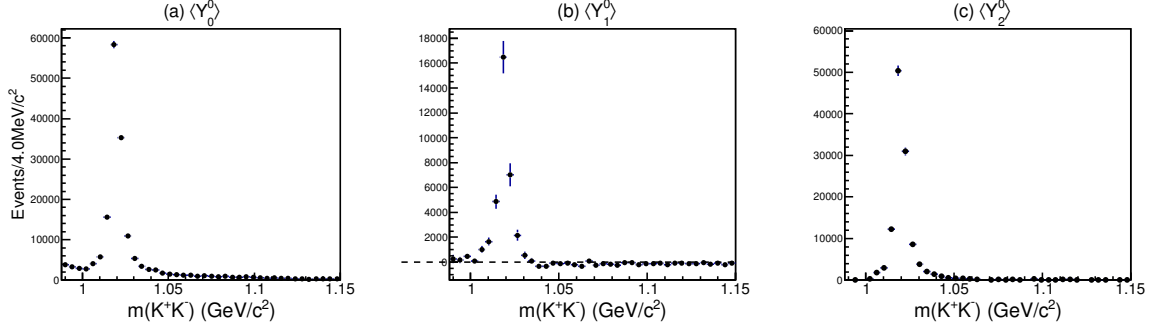


Figure 11:  $K^+K^-$  mass spectrum in the threshold region weighted by (a)  $Y_0^0$ , (b)  $Y_1^0$  and (c)  $Y_2^0$ , corrected for efficiency and phase space, and background subtracted.

2 The above system of equations can be solved in each interval of  $K^+K^-$  invariant mass for  $|S|$  and  $|P|$   
 3 and the resulting distributions are shown in Fig. 12.

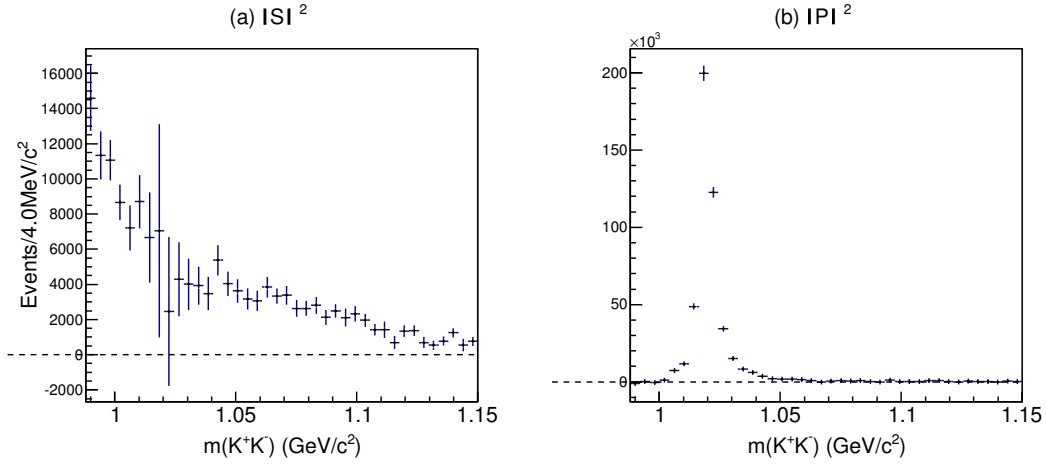


Figure 12: Squared (a) S- and (b) P-wave amplitudes

#### 4 4.4 S-wave Parameterization at the $K^+K^-$ Threshold

5 We empirically parameterize the  $S(980)$  with the following function:

$$A_{S(980)} = \frac{1}{m_0^2 - m^2 - im_0\Gamma_0\rho_{KK}},\tag{11}$$

6 where  $\rho_{KK} = 2p/m$ , and obtain the following parameter values by fitting the S-wave amplitudes in  
 7 Fig. 12 (b) with this Eq. 11.:

$$\begin{aligned}m_0 &= (0.919 \pm 0.006_{stat}) \text{ GeV}, \\ \Gamma_0 &= (0.272 \pm 0.040_{stat}) \text{ GeV}.\end{aligned}\tag{12}$$

1 The errors are statistical only. The fit result is shown in Fig. 13.

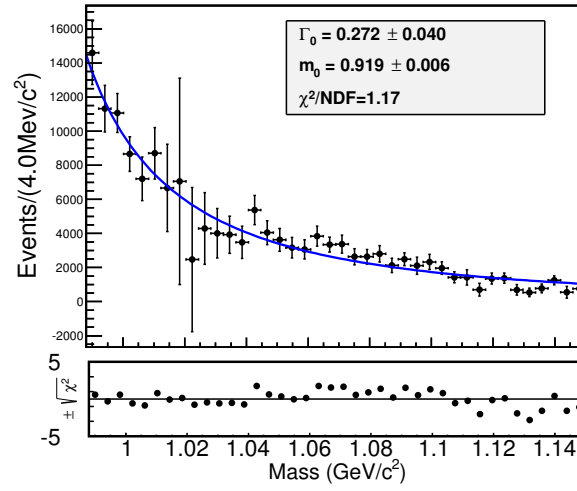


Figure 13: Fit of S-wave amplitudes. The curves result from the fit described in the text.

## 5 Amplitude Analysis

### 5.1 Event Selection

After  $K^\pm$ ,  $K_S^0$ ,  $\eta$ ,  $\eta'$ ,  $\pi^\pm$  and  $\pi^0$  are identified in Sec. 3, hadronic  $D_s$  decays can be reconstructed with the DTag package. Eight tag modes are used:

$$D_s^- \rightarrow K^+ K^- \pi^-, D_s^- \rightarrow K_S^0 K^-, D_s^- \rightarrow K_S^0 K^- \pi^+ \pi^-, D_s^- \rightarrow K^- \pi^+ \pi^-, D_s^- \rightarrow K_S^0 K^+ \pi^- \pi^-, D_s^- \rightarrow \pi^+ \pi^- \pi^-, D_s^- \rightarrow \eta_{\pi^+ \pi^- \eta_{\gamma\gamma}}', D_s^- \rightarrow K^+ K^- \pi^- \pi^0.$$

With the tagged  $D_s$  meson, the signal  $D_s$  is reconstructed with the remaining good tracks. The momentum of  $\pi^\pm$  ( $\pi^0$ ) is required to be larger than 100 MeV/c<sup>2</sup> to suppress the background of  $D^* \rightarrow D\pi$ . Only the  $D_s$  candidate with invariant mass falls into [1.87, 2.06] GeV/c<sup>2</sup> are selected.

For every candidate of  $D_s D_s^*$  decays, all tracks at signal side and tag side as well as gamma from  $D_s^*$  are added to apply kinematic fitting. Five constrains are added in kinematic fitting: four-momentum of  $D_s D_s^*$  and mass of  $D_s^*$ . Then we select the candidate with minimum  $\chi_{5c}^2$ .

The candidates satisfy:

- $m_{sig}$  and  $m_{tag}$  falls in the mass regions shown in Table 4,
- $\chi_{5c}^2 < 200$ ,

are retained for the amplitude analysis, where  $m_{sig}$  and  $m_{tag}$  refer to mass of  $D_s$  at signal side and tag side respectively.

Table 4: The mass windows for each tag mode. The mass windows use the results in Ref. [14]

Tag mode	Mass window (GeV/c <sup>2</sup> )
$D_s^- \rightarrow K_S^0 K^-$	[1.948, 1.991]
$D_s^- \rightarrow K^+ K^- \pi^-$	[1.900, 2.030]
$D_s^- \rightarrow K^+ K^- \pi^- \pi^0$	[1.947, 1.982]
$D_s^- \rightarrow K_S^0 K^- \pi^+ \pi^-$	[1.958, 1.980]
$D_s^- \rightarrow K_S^0 K^+ \pi^- \pi^-$	[1.953, 1.983]
$D_s^- \rightarrow \pi^- \pi^- \pi^+$	[1.952, 1.984]
$D_s^- \rightarrow \pi^- \eta_{\pi^+ \pi^- \eta_{\gamma\gamma}}'$	[1.940, 1.996]
$D_s^- \rightarrow K^- \pi^+ \pi^-$	[1.953, 1.983]

### 5.2 Background Analysis

We use generic MC to estimate the background. The background and signal shape of generic MC is shown in Fig. 14. By scaling the generic MC background sample to the data size based on the luminosities, the background yields in the signal region is 17.2. The fit to the signal  $D_s$  invariant mass

- 1 ( $m_{sig}$ ) spectrum gives the background yield in the signal region is  $18.1 \pm 5.1$ , shown as in Fig. 15. The  
 2 background level in generic MC is consistent with the data. In the fit, the signal shape is the MC shape  
 3 convoluted with a Gaussian function and the background is the MC shape.

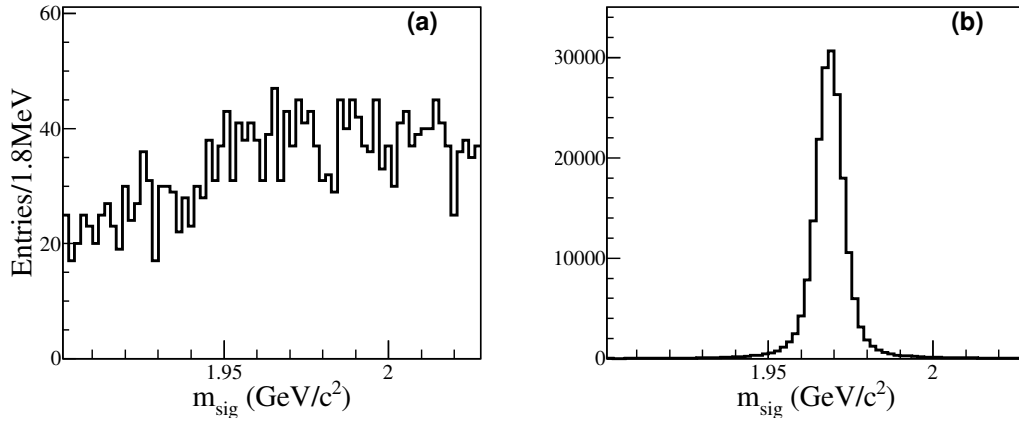


Figure 14: The background and the signal shape of generic MC (round 01-40)

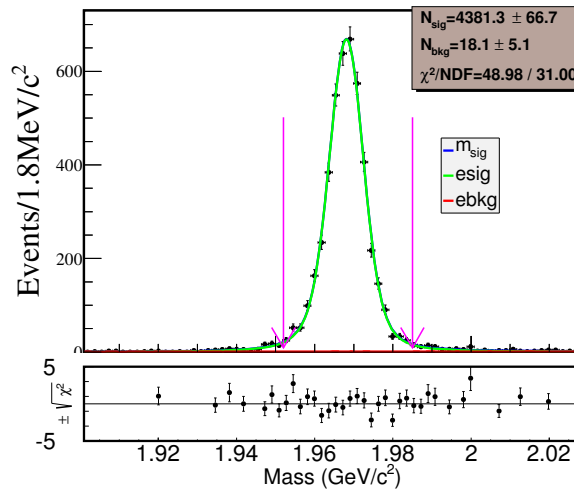


Figure 15: The fit to  $m_{sig}$  for data after selections, the area between the purple arrows is the signal area of the sample for the amplitude analysis.

### 4 5.3 Fit Method

5 The method used in the amplitude analysis is the same as the Ref. [15]. In this section, we briefly  
 6 review the amplitude analysis method used in this analysis.

7 The relative magnitudes and phases of the partial waves and the mass and width of intermediate  
 8 resonances are determined by an unbinned maximum-likelihood fit to the data selected. The formulas  
 9 are constructed with covariant tensors [16].

Since there are three final state particles, only one possible resonant state is allowed in any intermediate process. Thus the amplitude of the  $n^{\text{th}}$  intermediate state ( $A_n$ ) is,

$$A_n = P_n S_n F_n^r F_n^D, \quad (13)$$

where  $S_n$  and  $F_n^{r(D)}$  are the spin factor and the Blatt-Weisskopf barriers of the intermediate state (the  $D_s$  meson), respectively.  $P_n$  is the propagator of the intermediate resonance.

The total amplitude  $M$  is then the coherent sum of the amplitudes of intermediate processes,  $M = \sum c_n A_n$ , where  $c_n = \rho_n e^{i\phi_n}$  is the corresponding complex coefficient. The magnitude  $\rho_n$  and phase  $\phi_n$  are determined by the amplitude analysis. The signal probability density function (PDF)  $f_S(p_j)$  is given by

$$f_S(p_j) = \frac{\epsilon(p_j) |M(p_j)|^2 R_3(p_j)}{\int \epsilon(p_j) |M(p_j)|^2 R_3(p_j) dp_j}, \quad (14)$$

where  $\epsilon(p_j)$  is the detection efficiency parameterized in terms of the final four-momenta  $p_j$ . The index  $j$  refers to the different particles in the final states.  $R_3(p_j)$  is the standard element of the three-body phase space. The normalization integral is determined by a MC integration,

$$\int \epsilon(p_j) |M(p_j)|^2 R_3(p_j) dp_j \approx \frac{1}{N_{MC}} \sum_{k_{MC}}^{N_{MC}} \frac{|M(p_j^{k_{MC}})|^2}{|M^{gen}(p_j^{k_{MC}})|^2}, \quad (15)$$

where  $k_{MC}$  is the index of the  $k_{MC}^{\text{th}}$  event of the MC sample and  $N_{MC}$  is the number of the selected MC events.  $M^{gen}(p_j)$  is the PDF used to generate the MC samples in MC integration. At the beginning, the PHSP MC are used in MC integration.  $M^{gen}(p_j)$  is a constant overall the phase space. Then with the result obtained from the fit to data, the signal MC is then generated and used in MC integration. In this analysis, a PHSP MC sample with about 6 million events and a signal MC sample with about 2 million events are used in the normalization integral calculation using PHSP MC and signal MC, respectively. In the numerator of Eq .14,  $\epsilon(p_j)$  is independent of the fitted variables, so it is regarded as a constant term in the fit. Considering the bias caused by particle identification (PID) [20] and tracking [21] efficiency differences between data and MC, we introduce  $\gamma_\epsilon$  to correct this bias:

$$\gamma_\epsilon = \prod_i \frac{\epsilon_{i,data}(p_i)}{\epsilon_{i,MC}(p_i)}, \quad (16)$$

where  $i$  denotes the three daughter particles.

Since there is only about 0.4% background in the data sample, the contribution from the background is ignored in the likelihood calculation:

$$\ln L = \sum_k^{N_{data}} \ln f_S(p_j^k), \quad (17)$$

where  $N_{data}$  is the number of candidate events in data.

### 5.3.1 Propagator

For a decay process  $a \rightarrow bc$ ,  $s_{a/b/c}$  is denoted to be the invariant mass square of the particle a/b/c,  $r_a = p_b - p_c$ , and  $q$  is denoted as the magnitude of the momentum of daughter particle in the rest system of  $a$

$$q = \sqrt{\frac{(s_a + s_b + s_c)^2}{4s_a} - s_b}. \quad (18)$$

The intermediate resonances  $K^*(892)^0$ ,  $\phi(1020)$  and  $f_0(1710)$  are parameterized as a RBW,

$$P = \frac{1}{(m_0^2 - s_a) - im_0\Gamma(m)}, \quad (19)$$

$$\Gamma(m) = \Gamma_0 \left(\frac{q}{q_0}\right)^3 \left(\frac{m_0}{m}\right) \left(\frac{X_L(q)}{X_L(q_0)}\right)^2,$$

where  $m_0$  and  $\Gamma_0$  are the mass and the width of the intermediate resonances, and are fixed to the PDG values [13] except the mass and the width of  $f_0(1370)$ . The mass and width of  $f_0(1370)$  are fixed to 1350 MeV/ $c^2$  and 265 MeV/ $c^2$  [17], respectively.. The value of  $q_0$  in Eq. 19 is that of  $q$  when  $s_a = m_0^2$ ,  $L$  denotes the angular momenta and  $X_L(q)$  is defined as:

$$\begin{aligned} X_{L=0}(q) &= 1, \\ X_{L=1}(q) &= \sqrt{\frac{2}{z^2+1}}, \\ X_{L=2}(q) &= \sqrt{\frac{13}{9z^4+3z^2+1}}, \end{aligned} \quad (20)$$

where  $z = qR$ . The  $R$  is the effective radius of the intermediate state or  $D_s$  meson and set to 3.0 GeV $^{-1}$  for intermediate states and 5.0 GeV $^{-1}$  for  $D_s$  meson [15], respectively. This value  $R$  is a typical value used by  $D$  physics and we will also vary this value as a source of systematical uncertainties.

$K_0^*(1430)^0$  is parameterized with Flatte formula:

$$P_{K_0^*(1430)^0} = \frac{1}{M^2 - s - i(g_1\rho_{K\pi}(s) + g_2\rho_{\eta'K}(s))}, \quad (21)$$

where  $s$  is the  $K^-\pi^+$  invariant mass squared,  $\rho_{K\pi}(s)$  and  $\rho_{\eta'K}(s)$  are Lorentz invariant PHSP factor, and  $g_{1,2}$  are coupling constants to the corresponding final state. The parameters of  $K_0^*(1430)^0$  are fixed to values measured by CLEO [18]. For resonances  $f_0(980)$  and  $a_0(980)$ , as is discussed in Sec. 1.1, we use Eq. 11 to describe the propagator and the values of parameters are fixed to the values in Eq. 12 obtained from the model independent partial wave analysis section (Sec. 4.4).

### 5.3.2 Blatt-Weisskopf Barriers

The Blatt-Weisskopf barriers are given by

$$\begin{aligned} F_n &= 1, & (S \text{ wave}), \\ F_n &= \sqrt{\frac{z_0^2+1}{z^2+1}}, & (P \text{ wave}), \\ F_n &= \sqrt{\frac{z_0^4+3z_0^2+9}{z^4+3z^2+9}}, & (D \text{ wave}), \end{aligned} \quad (22)$$

where  $z_0$  are  $qR$  and  $q_0R$ , respectively.

### 5.3.3 Spin Factors

As the limit of the phase space, we only consider the states with angular momenta no more than 2.

Considering a two-body decay, the spin projection operators are defined as

$$\begin{aligned} P^0(a) &= 1, & (S \text{ wave}), \\ P_{\mu\mu'}^{(1)}(a) &= -g_{\mu\mu'} + \frac{p_{a,\mu}p_{a,\mu'}}{p_a^2}, & (P \text{ wave}), \\ P_{\mu\nu\mu'\nu'}^{(2)}(a) &= \frac{1}{2}(P_{\mu\mu'}^{(1)}(a)P_{\nu\nu'}^{(1)}(a) + P_{\mu\nu'}^{(1)}(a)P_{\nu\mu'}^{(1)}(a)) + \frac{1}{3}P_{\mu\nu}^{(1)}(a)P_{\mu'\nu'}^{(1)}(a), & (D \text{ wave}). \end{aligned} \quad (23)$$

The covariant tensors are given by

$$\begin{aligned} \tilde{t}^{(0)}(a) &= 1, & (S \text{ wave}), \\ \tilde{t}_\mu^{(1)}(a) &= -P_{\mu\mu'}^{(1)}(a)r^{\mu'}, & (P \text{ wave}), \\ \tilde{t}_{\mu\nu}^{(2)}(a) &= P_{\mu\nu\mu'\nu'}^{(2)}(a)r_a^{\mu'}r_a^{\nu'}, & (D \text{ wave}). \end{aligned} \quad (24)$$

The spin factor for  $D_s \rightarrow aX$  and then  $a \rightarrow bc$  is ( $a$  refers to the intermediate resonance),

$$\begin{aligned} S_n &= 1, & (S \text{ wave}), \\ S_n &= \tilde{T}^{(1)\mu}(D_s)\tilde{t}_\mu^{(1)}(a), & (P \text{ wave}), \\ S_n &= \tilde{T}^{(2)\mu}(D_s)\tilde{t}_\mu^{(2)}(a), & (D \text{ wave}), \end{aligned} \quad (25)$$

where the  $\tilde{T}^{(1)\mu}(D_s)$  ( $\tilde{T}^{(2)\mu}(D_s)$ ) and  $\tilde{t}_\mu^{(1)}(a)$  ( $\tilde{t}_\mu^{(2)}(a)$ ) are the same defined in Ref. [16].

### 5.4 Fit Fraction

The fit fractions of the individual amplitudes are calculated according to the fit results and are compared to the other measurements. In the calculation, a PHSP MC with neither detector acceptance nor resolution is involved. The fit fraction for an amplitude is defined as

$$FF(n) = \frac{\sum_{k=1}^{N_{gen}} |A_n|^2}{\sum_{k=1}^{N_{gen}} |M(p_j^k)|^2}, \quad (26)$$

where  $N_{gen} = 2000000$ , is the number of the PHSP MC events at generator level.

To estimate the statistical uncertainties of the fit fractions, we repeat the calculation of fit fractions by randomly varying the fitted parameters according to the error matrix. Then, for each amplitude, we fit the resulting distribution with a Gaussian function, whose width gives the corresponding statistical uncertainty.

### 5.5 Fit Result

The Dalitz plot of  $m^2(K^+K^-)$  versus  $m^2(K^-\pi^+)$  is shown in Fig. 16. In the plot, we can see a clear peak of  $K^*(892)^0$  and  $\phi(1020)$ . In the fit, the magnitude and phase of the amplitude  $D_s^+ \rightarrow K^*(892)^0 K^+$  is fixed to 1.0 and 0.0, and the magnitudes and phases of the amplitudes are allowed to float.

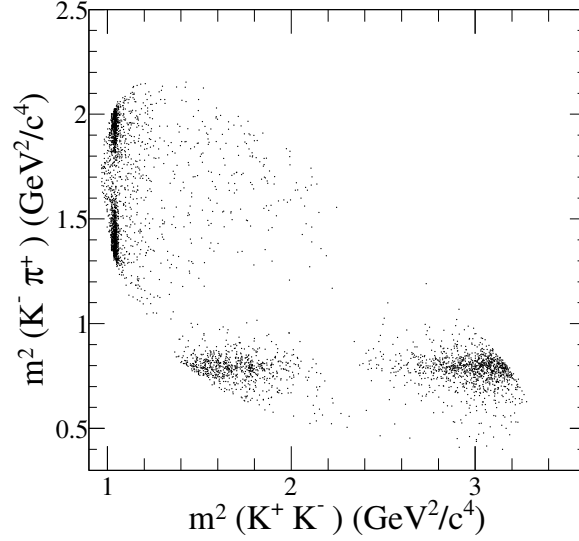


Figure 16: The Dalitz plot of  $m^2(K^- \pi^+)$  versus  $m^2(K^+ K^-)$  after event selection.

With the requiring the statistical significance larger than 5 standard deviations, there are 6 intermediate process,  $D_s^+ \rightarrow \bar{K}^*(892)^0 K^+$ ,  $D_s^+ \rightarrow \phi(1020)\pi^+$ ,  $D_s^+ \rightarrow S(980)\pi^+$ ,  $D_s^+ \rightarrow \bar{K}_0^*(1430)^0 K^+$ ,  $D_s^+ \rightarrow f_0(1370)\pi^+$ ,  $D_s^+ \rightarrow f_0(1710)\pi^+$  are retained in the final result. The statistical significance of the three amplitudes in final result are also checked. The statistical significance is calculated by the difference of the likelihood of fits with and without a certain amplitude along with the difference of degree of freedom. The detail  $\Delta(\ln L)$ ,  $\Delta n_{par}$ , and the statistical significance for each amplitude are listed in Table 5. We also tested some other intermediate resonances. With each tested amplitude added and fit repeated, we get the corresponding likelihood shift ( $\Delta(\ln L)$ ), the number of freedom degree shift ( $\Delta n_{par}$ ) and the statistical significance, and the results are listed in Table 6. All tested amplitudes in Table 6 with statistical significances less than 5 are not retained.

Table 5: The  $\Delta(\ln L)$ ,  $\Delta n_{par}$ , and the statistical significance for each amplitude

Amplitude	$\Delta(\ln L)$	$\Delta n_{par}$	Stat. significance
$D_s^+ \rightarrow \bar{K}^*(892)^0 K^+$	1959.3	2	>20
$D_s^+ \rightarrow \phi(1020)\pi^+$	2303.3	2	>20
$D_s^+ \rightarrow S(980)\pi^+$	270.5	2	>20
$D_s^+ \rightarrow \bar{K}_0^*(1430)^0 K^+$	39.4	2	8.6
$D_s^+ \rightarrow f_0(1710)\pi^+$	44.7	2	9.2
$D_s^+ \rightarrow f_0(1370)\pi^+$	22.5	2	6.4

The magnitudes, phases, and fit fractions for the six amplitudes are listed in Table 7.



Table 6: The  $\Delta(\ln L)$ ,  $\Delta n_{par}$ , and the statistical significance for tested amplitudes

Amplitude	$\Delta(\ln L)$	$\Delta n_{par}$	Stat. significance
$D_s^+ \rightarrow f_0(1500)\pi^+$	0.8	2	0.8
$D_s^+ \rightarrow \phi(1680)\pi^+$	1.8	2	1.4
$D_s^+ \rightarrow f_2(1270)\pi^+$	4.5	2	2.5
$D_s^+ \rightarrow f_2(1525)\pi^+$	0.2	2	0.2
$D_s^+ \rightarrow \bar{K}_1^*(1410)^0 K^+$	4.8	2	2.6
$D_s^+ \rightarrow \bar{K}_1^*(1680)^0 K^+$	0.1	2	0.1
$D_s^+ \rightarrow \bar{K}_2^*(1430)^0 K^+$	2.8	2	1.9
non-resonance	6.4	2	3.1

Table 7: The magnitudes, phases and fit fractions for the six amplitudes

Amplitude	Magnitude	Phase	Fit fractions(%)
$D_s^+ \rightarrow \bar{K}^*(892)^0 K^+$	1.0(fixed)	0.0(fixed)	48.3 $\pm$ 0.9
$D_s^+ \rightarrow \phi(1020)\pi^+$	1.09 $\pm$ 0.02	6.22 $\pm$ 0.07	40.5 $\pm$ 0.7
$D_s^+ \rightarrow S(980)\pi^+$	2.88 $\pm$ 0.14	4.77 $\pm$ 0.07	19.3 $\pm$ 1.7
$D_s^+ \rightarrow \bar{K}_0^*(1430)^0 K^+$	1.26 $\pm$ 0.14	2.91 $\pm$ 0.20	3.0 $\pm$ 0.6
$D_s^+ \rightarrow f_0(1710)\pi^+$	0.79 $\pm$ 0.08	1.02 $\pm$ 0.12	1.9 $\pm$ 0.4
$D_s^+ \rightarrow f_0(1370)\pi^+$	0.58 $\pm$ 0.08	0.59 $\pm$ 0.17	1.2 $\pm$ 0.4

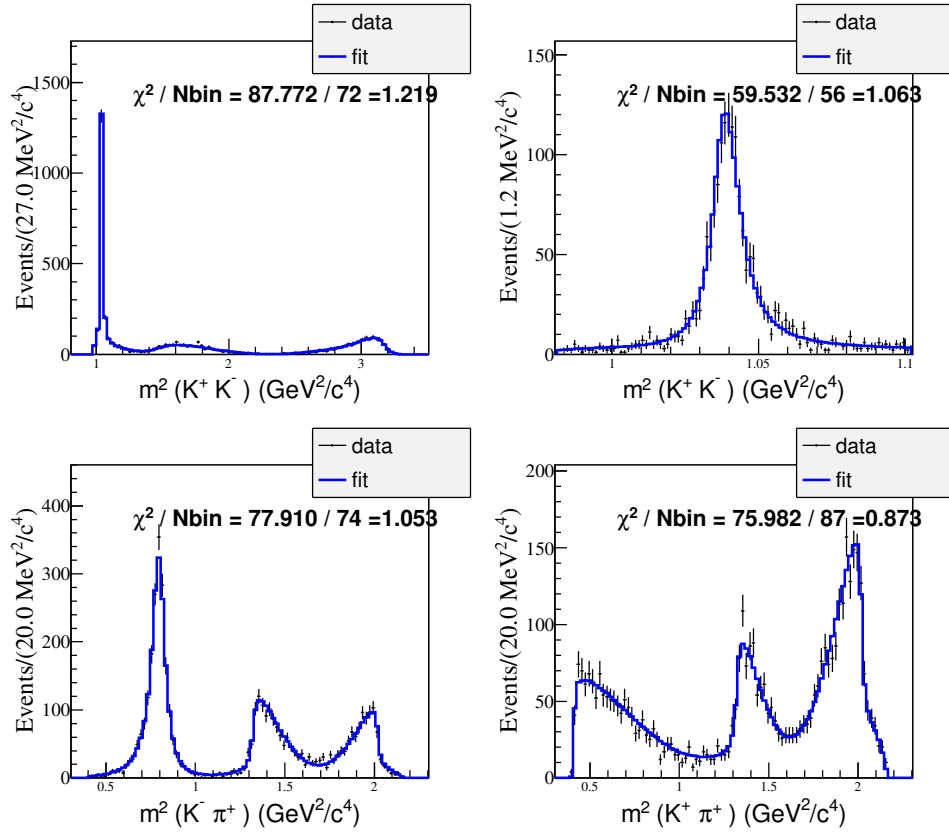


Figure 17:  $D_s^+ \rightarrow K^+ K^- \pi^+$ : Dalitz plot projections from the nominal fit. The data are represented by points with error bars, the fit results by the histograms.

Table 8: The results of pull distribution checks for the magnitudes, phases and fit fractions for different amplitudes.

Amplitude	Phase		Magnitude		Fit fraction	
	mean	width	mean	width	mean	width
$D_s^+ \rightarrow \bar{K}^*(892)^0 K^+$					$-0.13 \pm 0.04$	$0.98 \pm 0.03$
$D_s^+ \rightarrow \phi(1020)\pi^+$	$-0.04 \pm 0.05$	$1.00 \pm 0.03$	$0.07 \pm 0.04$	$0.95 \pm 0.03$	$0.01 \pm 0.04$	$0.95 \pm 0.03$
$D_s^+ \rightarrow S(980)\pi^+$	$-0.07 \pm 0.05$	$1.01 \pm 0.03$	$0.07 \pm 0.05$	$1.10 \pm 0.04$	$0.02 \pm 0.05$	$1.14 \pm 0.04$
$D_s^+ \rightarrow \bar{K}_0^*(1430)^0 K^+$	$0.00 \pm 0.05$	$1.11 \pm 0.04$	$0.14 \pm 0.04$	$0.95 \pm 0.03$	$0.10 \pm 0.04$	$0.99 \pm 0.03$
$D_s^+ \rightarrow f_0(1710)\pi^+$	$0.00 \pm 0.04$	$0.98 \pm 0.03$	$0.08 \pm 0.04$	$0.97 \pm 0.03$	$0.01 \pm 0.04$	$0.99 \pm 0.03$
$D_s^+ \rightarrow f_0(1370)\pi^+$	$-0.11 \pm 0.05$	$1.10 \pm 0.04$	$0.21 \pm 0.04$	$0.99 \pm 0.03$	$0.15 \pm 0.04$	$0.98 \pm 0.03$

The Dalitz plot projections are shown in Fig. 17. The fit quality is determined by calculating the  $\chi^2$  of the fit using an adaptive binning of the  $m^2(K^+ K^-)$  versus  $m^2(K^- \pi^+)$  Dalitz plot that requires each bin contains at least 10 events. The goodness of the nominal fit is  $\chi^2 = 290.1/280 = 1.04$ .

## 5.6 Systematic Uncertainties

Systematic uncertainties take in account:

- I Variation of masses and widths of resonances within one  $\sigma$  error.
  - For  $S(980)$ , the mass and width are shifted within errors from Eq. 12 in Sec. 4.4.
  - For  $f_0(1370)$ , the mass and width are shifted within errors from Ref. [17].
  - For other states, uncertainties are taken from PDG [13].
- II Variation of the effective radius of Blatt-Weisskopf Barrier within the range  $[1.0, 5.0] \text{ GeV}^{-1}$  for intermediate resonances and  $[3.0, 7.0] \text{ GeV}^{-1}$  for  $D_s$  mesons.
- III Fit bias. The possible bias is given by the result from pull distribution check. With the results obtained from the fit, the signal MC samples are generated with the same size of the data. In this analysis, 300 MC samples with the size equaling to data are used to perform the pull distribution check. The results are listed in Table 8. The corresponding plots are shown in Fig. 18, Fig. 19 and Fig. 20.
- IV Experimental effects. The experimental effects are related to the acceptance difference between MC and data caused by PID and tracking efficiencies, that is  $\gamma_\epsilon$  in Eq. 16. To estimate the uncertainties caused by  $\gamma_\epsilon$ , the amplitude fit is performed varying PID and tracking efficiencies according to their uncertainties.

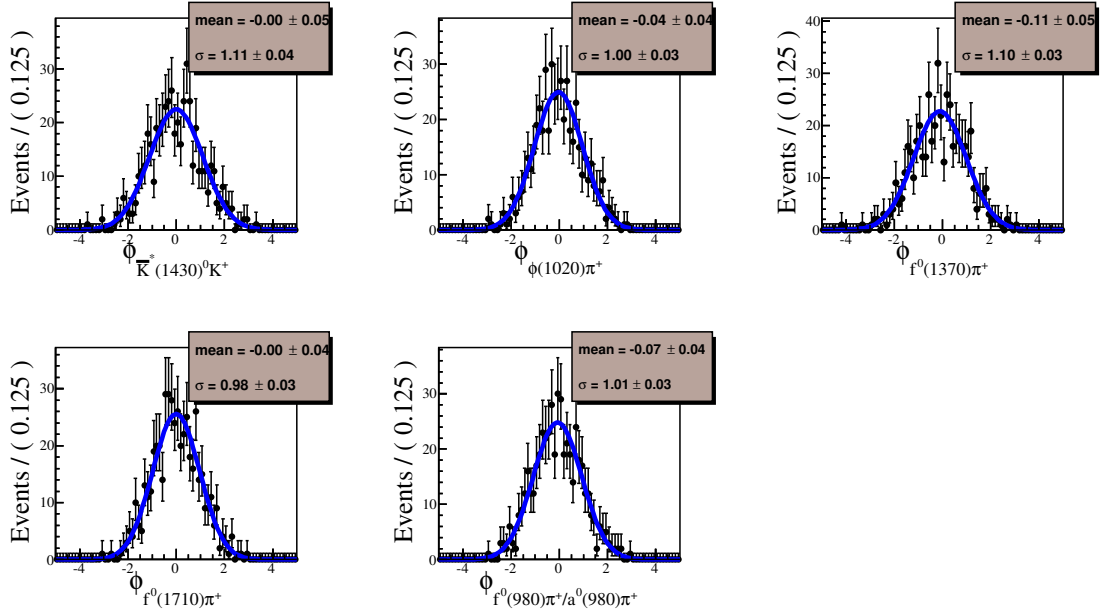


Figure 18: The pull distribution check results for phases of the amplitudes in the nominal fit model.

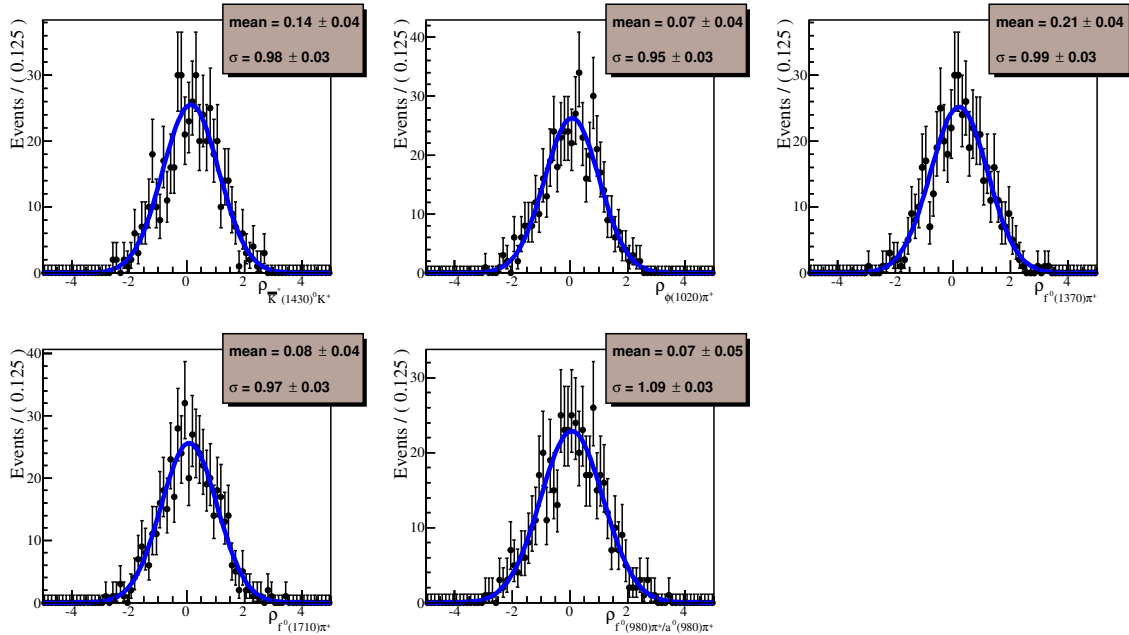


Figure 19: The pull distribution check results for magnitudes of the amplitudes in the nominal fit model.

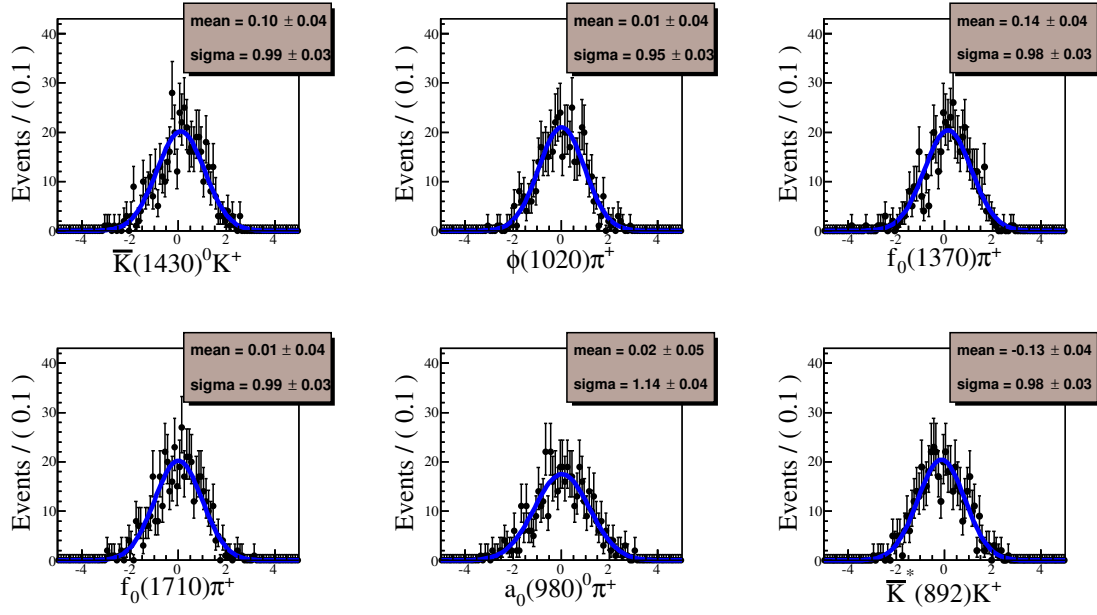


Figure 20: The pull distribution check results for fit fractions of the amplitudes in the nominal fit model.

- 1 The detail results of the systematic uncertainties are summarized in Table 9. The final results of the
- 2 amplitude analysis are then listed in Table 10.

Table 9: Systematic uncertainties on the  $\phi$  and FFs for different amplitudes in units of the corresponding statistical uncertainties.

Amplitude		Source				Total
		I	II	III	IV	
$D_s^+ \rightarrow \bar{K}^*(892)^0 K^+$	FF	0.32	0.29	0.13	0.41	0.61
	$\phi$	0.49	0.10	0.06	0.07	0.51
$D_s^+ \rightarrow \phi(1020)\pi^+$	$\rho$	0.49	0.14	0.18	0.41	0.68
	FF	0.44	1.13	0.05	0.40	1.28
	$\phi$	0.98	0.25	0.06	0.11	1.02
$D_s^+ \rightarrow S(980)\pi^+$	$\rho$	1.11	0.17	0.10	0.11	1.13
	FF	1.16	0.15	0.06	0.09	1.18
	$\phi$	1.02	0.48	0.09	0.21	1.15
$D_s^+ \rightarrow \bar{K}_0^*(1430)^0 K^+$	$\rho$	1.00	0.36	0.13	0.20	1.09
	FF	0.76	0.35	0.11	0.22	0.87
	$\phi$	0.31	0.25	0.09	0.14	0.43
$D_s^+ \rightarrow f_0(1710)\pi^+$	$\rho$	1.17	1.23	0.07	0.11	1.70
	FF	0.71	1.21	0.05	0.16	1.42
	$\phi$	2.66	0.27	0.11	0.09	2.68
$D_s^+ \rightarrow f_0(1370)\pi^+$	$\rho$	1.01	0.32	0.06	0.09	1.06
	FF	0.42	0.30	0.15	0.06	0.54
	$\phi$	0.42	0.30	0.15	0.06	0.54

Table 10: The final results of the magnitudes, phases and fit fractions for the six amplitudes. The first and second uncertainties are the statistical and systematic uncertainties, respectively.

Amplitude	Magnitude	Phase	Fit fractions (%)
$D_s^+ \rightarrow \bar{K}^*(892)^0 K^+$	1.0 (fixed)	0.0 (fixed)	$48.3 \pm 0.9 \pm 0.5$
$D_s^+ \rightarrow \phi(1020)\pi^+$	$1.09 \pm 0.02 \pm 0.01$	$6.22 \pm 0.07 \pm 0.04$	$40.5 \pm 0.7 \pm 0.9$
$D_s^+ \rightarrow S(980)\pi^+$	$2.88 \pm 0.14 \pm 0.16$	$4.77 \pm 0.07 \pm 0.07$	$19.3 \pm 1.7 \pm 2.0$
$D_s^+ \rightarrow \bar{K}_0^*(1430)^0 K^+$	$1.26 \pm 0.14 \pm 0.15$	$2.91 \pm 0.20 \pm 0.23$	$3.0 \pm 0.6 \pm 0.5$
$D_s^+ \rightarrow f_0(1710)\pi^+$	$0.79 \pm 0.08 \pm 0.14$	$1.02 \pm 0.12 \pm 0.05$	$1.9 \pm 0.4 \pm 0.6$
$D_s^+ \rightarrow f_0(1370)\pi^+$	$0.58 \pm 0.08 \pm 0.08$	$0.59 \pm 0.17 \pm 0.46$	$1.2 \pm 0.4 \pm 0.2$

## 6 Branching Fraction Measurements

### 6.1 Event Selection

After the selection described in Sec. 3, we further use the double tag technique for the branching fraction measurement. We use the same 8 tag modes as in Sec. 5.1. In the selection of tag  $D_s$ , for multiple candidates, the best candidate is chosen with  $M_{rec}$  closest to mass of  $D_s^*$  in [13]. To further remove the background associated with the larger number of soft  $\pi^\pm$  ( $\pi^0$ ) from  $D_s^*$  decays, candidates are voted if the momentum of  $\pi^\pm$  ( $\pi^0$ ) is less than 0.1 GeV.

The single tag (ST) yields are extracted from the fits to the  $D_s$  invariant mass distributions, as shown in Fig. 21. In the fit, the mass windows of the tag modes are set to be the same as the Ref. [14]. The signal shape is modeled as MC shape convoluted with a Gaussian function, while background is parameterized as the 2nd-order Chebychev polynomial. The corresponding ST efficiencies are estimated from generic MC. The ST yields ( $Y_{ST}$ ) and ST efficiencies ( $\epsilon_{ST}$ ) are listed in Table 11.

Table 11: The ST yields ( $Y_{ST}$ ) and ST efficiencies ( $\epsilon_{ST}$ ). The mass windows use the results in Ref. [14]

Tag mode	Mass window (GeV/ $c^2$ )	$Y_{ST}$	$\epsilon_{ST}(\%)$
$D_s^- \rightarrow K_S^0 K^-$	[1.948, 1.991]	$965265 \pm 1286$	$49.48 \pm 0.07$
$D_s^- \rightarrow K^+ K^- \pi^-$	[1.900, 2.030]	$4254481 \pm 2947$	$42.17 \pm 0.03$
$D_s^- \rightarrow K^+ K^- \pi^- \pi^0$	[1.947, 1.982]	$1161036 \pm 3400$	$10.61 \pm 0.03$
$D_s^- \rightarrow K_S^0 K^- \pi^+ \pi^-$	[1.958, 1.980]	$233225 \pm 1467$	$19.30 \pm 0.12$
$D_s^- \rightarrow K_S^0 K^+ \pi^- \pi^-$	[1.953, 1.983]	$484801 \pm 1312$	$22.72 \pm 0.06$
$D_s^- \rightarrow \pi^- \pi^- \pi^+$	[1.952, 1.984]	$1152623 \pm 3370$	$56.94 \pm 0.17$
$D_s^- \rightarrow \pi^- \eta_{\pi^+ \pi^- \eta_{\gamma\gamma}}'$	[1.940, 1.996]	$251617 \pm 737$	$20.43 \pm 0.06$
$D_s^- \rightarrow K^- \pi^+ \pi^-$	[1.953, 1.983]	$610925 \pm 2902$	$47.18 \pm 0.22$

After a tag is identified, we search for the  $D_s^+ \rightarrow K^+ K^- \pi^+$  signal process. For each tag mode, we may have duplicate signal candidates and the candidates with the minimum average mass ( $aM$ ) of tag  $D_s$  and signal  $D_s$  are retained.

With the updated MC sample (DIY MC) based on the amplitude analysis results, the double efficiencies are determined and listed in Table 12.

### 6.2 Analytic Strategy

The data sample for this analysis is collected at  $E_{cm} = 4.178$  GeV, about 100 MeV higher than  $D_s^* D_s$  threshold. Around this energy region, based on the cross section measurement by CLEO [11], we know that most  $D_s$  production in  $e^+ e^-$  collision comes from  $D_s^{*\pm} D_s^\mp$  events with a cross section approximate

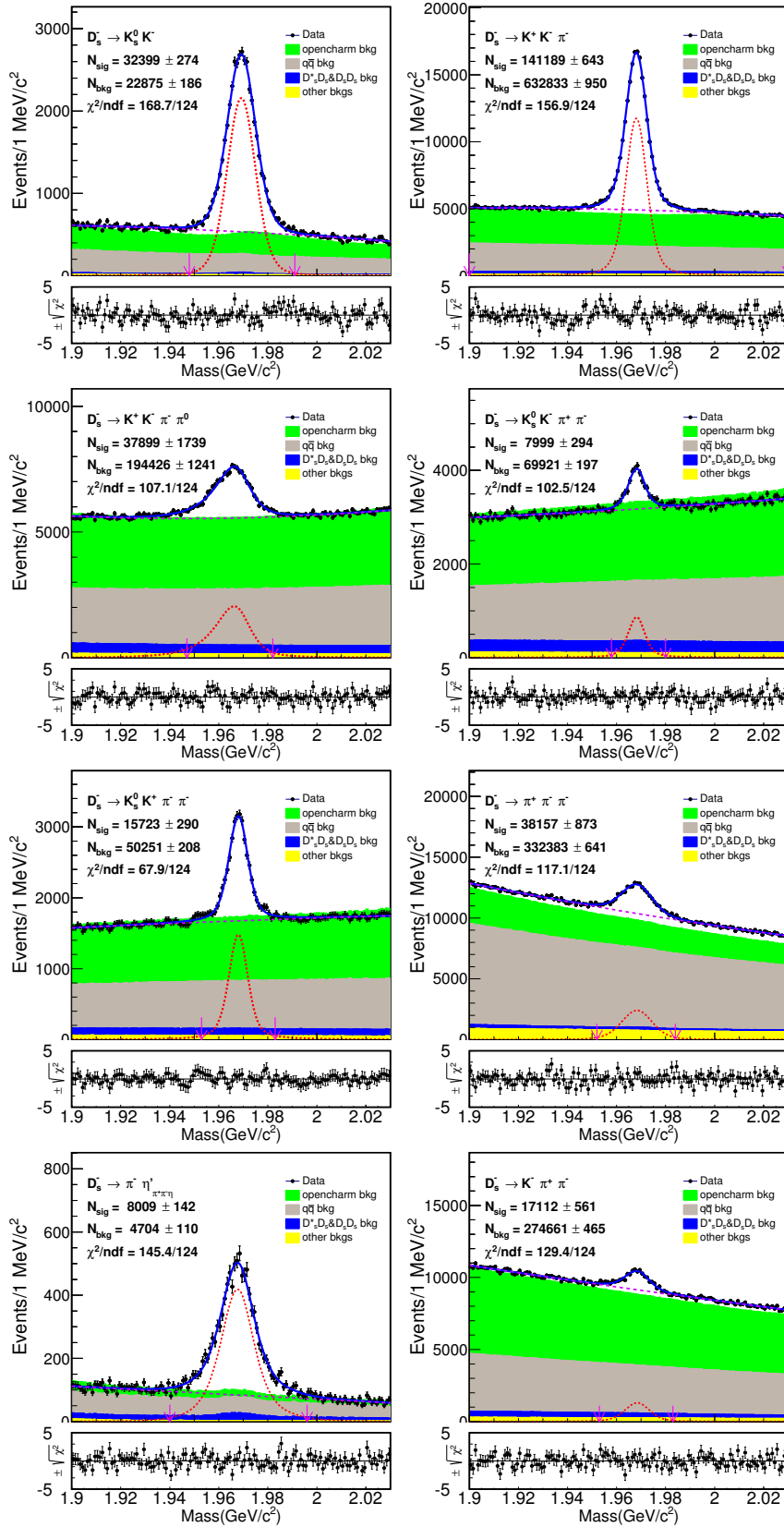


Figure 21:  $D_s$  Mass fits from data. The points with error bars are data, and the blue line is the fit. Red short-dashed lines are signal, violet long-dashed lines are background. The red arrows denote the signal region.



Table 12: The DT efficiencies ( $\epsilon_{DT}$ ).

Tag mode	$\epsilon_{DT}(\%)$
$D_s^- \rightarrow K_S^0 K^-$	$19.77 \pm 0.14$
$D_s^- \rightarrow K^+ K^- \pi^-$	$18.21 \pm 0.06$
$D_s^- \rightarrow K^+ K^- \pi^- \pi^0$	$4.69 \pm 0.03$
$D_s^- \rightarrow K_S^0 K^- \pi^+ \pi^-$	$8.34 \pm 0.11$
$D_s^- \rightarrow K_S^0 K^+ \pi^- \pi^-$	$9.55 \pm 0.09$
$D_s^- \rightarrow \pi^- \pi^- \pi^+$	$23.72 \pm 0.15$
$D_s^- \rightarrow \pi^- \eta'_{\pi^+ \pi^- \eta_{\gamma\gamma}}$	$8.70 \pm 0.11$
$D_s^- \rightarrow K^- \pi^+ \pi^-$	$19.68 \pm 0.17$

1 nb, while the cross section for  $D_s^+ D_s^-$  is about a factor of 20 smaller. The  $D_s^*$  decays to either  $\gamma D_s$  or  $\pi^0 D_s$  with branching fractions of  $(93.5 \pm 0.7)\%$  and  $(5.8 \pm 0.7)\%$  [13], respectively. The other charm productions have a total cross section of 8 nb. The underlying light quark “continuum” background is about 14 nb. The relatively large cross sections, relatively large branching fractions, and sufficient luminosities allow us to employ double tag (DT) technique to study this study.

As  $D_s^- \rightarrow K^+ K^- \pi^-$  is not only our signal mode but also one of our tag modes, we divide the events into two categories:

- Cat. A: Tag  $D_s$  decays to tag modes except  $D_s^- \rightarrow K^+ K^- \pi^-$ . The generic MC sample with the signal removed shows no peaking background around the fit range of  $1.90 < M_{sig} < 2.03 \text{ GeV}/c^2$ . Thus, the double tag yield is determined by the fit to  $M_{sig}$ , shown in Fig. 22(a). The background is described with  $2^{nd}$ -order Chebychev polynomial. The double tag yield is  $3484 \pm 64$ .
- Cat. B: Tag  $D_s$  decays  $K^+ K^- \pi^+$ . As both of the two  $D_s$  mesons decay to our signal modes, we fit  $aM$  (the average mass of  $D_s$  at signal side and tag side), which is shown in Fig. 22(b). Here, the background is described by a  $2^{nd}$ -order Chebychev polynomial. The double tag yield is  $1651 \pm 42$ .

To measure the branching fraction of this decay, we start from the following equations with one tag mode:

$$N_{tag}^{obs} = 2N_{D_s^+ D_s^-} \mathcal{B}_{tag} \epsilon_{tag}, \quad (27)$$

$$\begin{aligned} N_{sig}^{obsA} &= 2N_{D_s^+ D_s^-} \mathcal{B}_{tag} \mathcal{B}_{sig} \epsilon_{tag, sig}, & \text{for Cat. A} \\ N_{sig}^{obsB} &= N_{D_s^+ D_s^-} \mathcal{B}_{tag} \mathcal{B}_{sig} \epsilon_{tag, sig}, & \text{for Cat. B} \end{aligned} \quad (28)$$

where  $N_{D_s^+ D_s^-}$  is the total number of  $D_s^{*\pm} D_s^\mp$  produced from  $e^+ e^-$  collision;  $N_{tag}^{obs}$  is the number of observed tag modes;  $N_{sig}^{obsA}$  and  $N_{sig}^{obsB}$  are the number of observed signals for Cat. A and Cat. B, respectively;  $\mathcal{B}_{tag}$

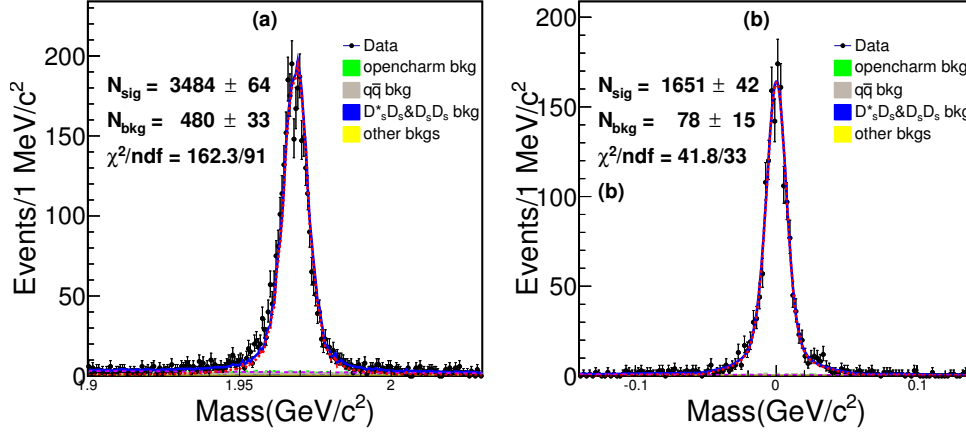


Figure 22: Fit of (a)Cat. A and (b)Cat. B. We fit  $M_{sig}$  and  $aM$  for Cat. A and Cat. B, respectively. The signal shapes are the corresponding simulated shapes convoluted with a Gaussian function and the background shapes are described with  $2^{nd}$ -order Chebychev polynomial.

1 and  $\mathcal{B}_{sig}$  are the branching fractions of a specific tag mode and the signal mode, respectively;  $\epsilon_{tag}$  is the  
 2 efficiency to reconstruct the tag mode;  $\epsilon_{tag,sig}$  is the efficiency to reconstruct both the tag and signal decay  
 3 modes.

4 Using the above equations, it's easy to obtain:

$$\mathcal{B}_{sig} = \frac{N_{sig}^{obsA} + 2N_{sig}^{obsB}}{\sum_{\alpha} N_{tag}^{\alpha} \epsilon_{tag,sig}^{\alpha} / \epsilon_{tag}^{\alpha}}, \quad (29)$$

5 where the yields  $N_{tag}^{obsA}$ ,  $N_{tag}^{obsB}$  and  $N_{tag}^{\alpha}$  are obtained from data, while  $\epsilon_{tag}$  and  $\epsilon_{tag,sig}$  can be obtained  
 6 from the appropriate MC samples, where  $\alpha$  represents the tag modes.

### 7 6.3 Results of Branching Fraction

8 We determine the branching fraction  $\mathcal{B}(D_s^+ \rightarrow K^+ K^- \pi^+) = (5.47 \pm 0.07)\%$  (statistical uncertainty  
 9 only) according to Eq. 29.

### 10 6.4 Systematic Uncertainties

11 The following sources are taken in account to calculate systematic uncertainties.

- 12 • Signal shape. The systematic uncertainty due to the signal shape is studied with the fit without the  
 13 Gaussian function convoluted, the double tag yield shift is taken as the related effect.
- 14 • Background shape and fit range. For background shape and the fit range, the MC shape is used to  
 15 replace the  $1^{st}$ -order Chebychev polynomial and the fit range of  $[1.90, 2.03] \text{ GeV}/c^2$  is changed to  
 16  $[1.89, 2.04] \text{ GeV}/c^2$ . The largest branching fraction shift is taken as the related effect.

- Fit bias. The possible bias is estimated by the input/output check using the round 30-40 of generic MC, which is shown in Table 13. The estimated mean ( $\mu_{\mathcal{B}}$ ) and its uncertainty ( $\sigma_{\mu}$ ) is calculated with the following formulas:

$$\mu_{\mathcal{B}} = \frac{\sum_i \frac{\mu_i}{\sigma_i^2}}{\sum_i \frac{1}{\sigma_i^2}}, \quad \sigma_{\mu}^2 = \sum_i \frac{1}{\sigma_i^2}, \quad (30)$$

where  $\mu_i$  and  $\sigma_i$  are the measured branching fraction value and its statistical uncertainty for the sample  $i$ . The combined result of the round 30-40 is  $\mu_{\mathcal{B}} = (5.462 \pm 0.021)\%$ . The relative change compared to the input value is 0.1%.

Table 13: input/output check using the round 30-40 of generic MC.

Round	$\mathcal{B}(D_s^+ \rightarrow K^+ K^- \pi^+)(\%)$
31	$5.562 \pm 0.066$
32	$5.497 \pm 0.066$
33	$5.407 \pm 0.066$
34	$5.636 \pm 0.068$
35	$5.490 \pm 0.066$
36	$5.397 \pm 0.066$
37	$5.369 \pm 0.066$
38	$5.490 \pm 0.067$
39	$5.353 \pm 0.065$
40	$5.435 \pm 0.066$
Combined result	$5.462 \pm 0.021$

- $K^{\pm}$  and  $\pi^{\pm}$  Tracking/PID efficiency. Based on the works [20] and [21] by Xingyu Shan and Sanqiang Qu, etc. we find that it's enough to assign 1.1% , 0.4%, 1.1% and 0.2% as the systematic uncertainty for  $K^{\pm}$  PID,  $\pi^{\pm}$  PID,  $K^{\pm}$  tracking,  $\pi^{\pm}$  tracking efficiencies, respectively.
- MC statistics. The uncertainty of MC statistics is obtained by  $\sqrt{\sum_i f_i \frac{\delta \epsilon_i}{\epsilon_i}}$ , where  $f_i$  is the tag yield fraction and  $\epsilon_i$  is the signal efficiency of tag mode  $i$ .

All of the systematic uncertainties mentioned above are summarized in Table 14.

The branching fraction with systematic uncertainties is  $\mathcal{B}(D_s^+ \rightarrow K^+ K^- \pi^+) = (5.47 \pm 0.07_{stat.} \pm 0.13_{sys.})\%$ .

Table 14: Systematic uncertainties of branching fraction.

Source	Sys. Uncertainty
Signal shape	0.3
Background shape and fit range	1.1
Fit bias	0.1
$K^\pm$ and $\pi^\pm$ PID efficiency	1.5
$K^\pm$ and $\pi^\pm$ Tracking efficiency	1.3
MC statistics	0.2
total	2.3

## 7 Summary

This analysis presents the amplitude analysis of the decay  $D_s^+ \rightarrow K^+ K^- \pi^+$ . Table 15 is a comparison of amplitude analysis between BABAR, CLEO-c and this analysis. Our results are roughly consistent with those of BABAR and CLEO-c. For the fit fraction of  $D_s^+ \rightarrow f_0(980)\pi^+ / a_0(980)\pi^+$ , we tend to agree with the result of BABAR.

Table 15: Comparison of fit fraction between BABAR, CLEO-c and this amplitude analysis.

Amplitude	BABAR	CLEO-c	This Analysis
$D_s^+ \rightarrow \bar{K}^*(892)^0 K^+$	$47.9 \pm 0.5 \pm 0.5$	$47.4 \pm 1.5 \pm 0.4$	$48.3 \pm 0.9 \pm 0.5$
$D_s^+ \rightarrow \phi(1020)\pi^+$	$41.4 \pm 0.8 \pm 0.5$	$42.2 \pm 1.6 \pm 0.3$	$40.5 \pm 0.7 \pm 0.9$
$D_s^+ \rightarrow S(980)\pi^+$	$16.4 \pm 0.7 \pm 2.0$	$28.2 \pm 1.9 \pm 1.8$	$19.3 \pm 1.7 \pm 2.0$
$D_s^+ \rightarrow \bar{K}_0^*(1430)^0 K^+$	$2.4 \pm 0.3 \pm 1.0$	$3.9 \pm 0.5 \pm 0.5$	$3.0 \pm 0.6 \pm 0.5$
$D_s^+ \rightarrow f_0(1710)\pi^+$	$1.1 \pm 0.1 \pm 0.1$	$3.4 \pm 0.5 \pm 0.3$	$1.9 \pm 0.4 \pm 0.6$
$D_s^+ \rightarrow f_0(1370)\pi^+$	$1.1 \pm 0.1 \pm 0.2$	$4.3 \pm 0.6 \pm 0.5$	$1.2 \pm 0.4 \pm 0.2$
$\sum FF(\%)$	$110.2 \pm 0.6 \pm 2.0$	$129.5 \pm 4.4 \pm 2.0$	$114.2 \pm 1.7 \pm 2.3$
$\chi^2/NDF$	$\frac{2843}{2305-14} = 1.2$	$\frac{178}{117} = 1.5$	$\frac{290}{291-10-1} = 1.04$
Events	$96307 \pm 369$ (purity 95%)	14400(purity 85%)	4381(purity 99.7%)

In this analysis, as  $a_0(980)$  and  $f_0(980)$  are close to each other and parameters of  $f_0(980)$  is not well measured, we have extracted the  $S$ -wave lineshape in the low end of  $K^+ K^-$  mass spectrum with the model independent method.

We also measure the branching fraction  $\mathcal{B}(D_s^+ \rightarrow K^+ K^- \pi^+) = (5.47 \pm 0.07_{stat.} \pm 0.13_{sys.})\%$ . As is shown in Table 16, the branching fraction of this analysis has the best precision.

Table 16: Comparisons of branching fraction between BABAR, CLEO-c and this analysis.

$\mathcal{B}(D_s^+ \rightarrow K^+ K^- \pi^+)(\%)$	Collaboration
$5.55 \pm 0.14_{stat.} \pm 0.13_{sys.}$	CLEO-c [22]
$5.06 \pm 0.15_{stat.} \pm 0.21_{sys.}$	BELLE [23]
$5.78 \pm 0.20_{stat.} \pm 0.30_{sys.}$	BABAR [24]
$5.47 \pm 0.07_{stat.} \pm 0.13_{sys.}$	BESIII(this analysis)

## References

- [1] Yu Lu and Liaoyuan Dong, BESIII DocDB 682-v7.
- [2] B. Aubert *et al.* (BABAR Collaboration), Phys. Rev. D **74**, 032003 (2006).
- [3] M. Ablikim *et al.* (BES2 Collaboration), Phys. Rev. D **72**, 092002 (2005).
- [4] V. V. Anisovich *et al.*, PAN **65** 1545 (2002).
- [5] H. Y. Cheng, Phys. Rev. D **67**, 094007 (2003).
- [6] H. Y. Cheng and C. W. Chiang, Phys. Rev. D **81**, 074031 (2010).
- [7] H. Y. Cheng, Phys. Lett. B **707**, 116 (2012).
- [8] P. L. Frabetti *et al.* (E687 Collaboration), Phys. Lett. B **351**, 591 (1995).
- [9] R. E. Mitchell *et al.* (CLEO Collaboration), Phys. Rev. D **79**, 072008 (2009).
- [10] P. del Amo Sanchez *et al.* (BARBAR Collaboration), Phys. Rev. D **83**, 052001 (2011).
- [11] D. Cronin-Hennessy *et al.* (CLEO Collaboration), Phys. Rev. D **80**, 072001 (2009).
- [12] Andy Julin, Hajime Muramatsu and Ron Poling, BESIII DocDB 580-v1.
- [13] K. A. Olive *et al.* (Particle Data Group), Chin. Phys. C **40**, 100001 (2016)
- [14] Sifan Zhang and Hailong Ma, BESIII DocDB 630-v35.
- [15] Yu Lu and Liaoyuan Dong, BESIII DocDB 416-v30.
- [16] B. S. Zou and D. V. Bugg, Eur. Phys. J. A **16**, 537 (2003).
- [17] M. Alblikim *et al.* (BESIII Collaboration), Phys. Lett. B **607** 243 (2005).
- [18] G. Bonvicini *et al.* (CLEO Collaboration), Phys. Rev. D **78**, 052001 (2001).
- [19] Yu Lu and Liaoyuan Dong, BESIII DocDB 613-v16.
- [20] <https://indico.ihep.ac.cn/event/8006/contribution/1/material/slides/0.pdf>
- [21] <https://indico.ihep.ac.cn/event/8023/contribution/1/material/slides/0.pdf>
- [22] P. U. E. Onyisi *et al.* (CLEO Collaboration), Phys. Rev. D **88**, 032009 (2013).

- <sup>1</sup> [23] A. Zupanc *et. al.* (BELLE Collaboration), JHEP **1309**, 139 (2013).
- <sup>2</sup> [24] P. del Amo Sanchez *et. al.* (BABAR Collaboration), Phys. Rev. D **82**, 091003 (2010).